



<b>Publication Year</b>	2021
<b>Acceptance in OA</b>	2022-06-06T10:24:58Z
<b>Title</b>	XMM-Newton campaign on the ultraluminous X-ray source NGC 247 ULX-1: outflows
<b>Authors</b>	PINTO, CIRO, Soria, R., Walton, D. J., D'Ai, A., Pintore, Fabio, Kosec, P., Alston, W. N., Fuerst, F., Middleton, M. J., Roberts, T. P., DEL SANTO, MELANIA, Barret, D., Ambrosi, E., Robba, A., Earnshaw, H., Fabian, A. C.
<b>Publisher's version (DOI)</b>	10.1093/mnras/stab1648
<b>Handle</b>	<a href="http://hdl.handle.net/20.500.12386/32182">http://hdl.handle.net/20.500.12386/32182</a>
<b>Journal</b>	MONTHLY NOTICES OF THE ROYAL ASTRONOMICAL SOCIETY
<b>Volume</b>	505

# XMM-*Newton* campaign on the ultraluminous X-ray source NGC 247 ULX-1: outflows

C. Pinto,<sup>1,2\*</sup> R. Soria,<sup>3</sup> D. J. Walton,<sup>4</sup> A. D’Ai,<sup>1</sup> F. Pintore,<sup>1</sup> P. Kosec,<sup>5</sup> W. N. Alston,<sup>6</sup> F. Fuerst,<sup>6</sup> M. J. Middleton,<sup>7</sup> T. P. Roberts,<sup>8</sup> M. Del Santo,<sup>1</sup> D. Barret,<sup>9</sup> E. Ambrosi,<sup>1</sup> A. Robba,<sup>1</sup> H. Earnshaw,<sup>10</sup> and A. C. Fabian<sup>4</sup>

<sup>1</sup>INAF - IASF Palermo, Via U. La Malfa 153, I-90146 Palermo, Italy

<sup>2</sup>ESTEC/ESA, Keplerlaan 1, 2201AZ Noordwijk, The Netherlands

<sup>3</sup>College of Astronomy and Space Sciences, University of the Chinese Academy of Sciences, Beijing 100049, China

<sup>4</sup>Institute of Astronomy, Madingley Road, CB3 0HA Cambridge, United Kingdom

<sup>5</sup>MIT Kavli Institute for Astrophysics and Space Research, Cambridge, MA 02139, USA

<sup>6</sup>ESAC/ESA European Space Astronomy Center, P.O. Box 78, 28691 Villanueva de la Canada, Madrid, Spain

<sup>7</sup>Physics & Astronomy, University of Southampton, Southampton, Hampshire SO17 1BJ, UK

<sup>8</sup>Centre for Extragalactic Astronomy, Durham University, Department of Physics, South Road, Durham DH1 3LE, UK

<sup>9</sup>Université de Toulouse, CNRS, IRAP, 9 Avenue du colonel Roche, BP 44346, 31028 Toulouse Cedex 4, France

<sup>10</sup>Cahill Center for Astronomy and Astrophysics, California Institute of Technology, Pasadena, CA 91125, USA

Accepted 2021 June 3. Received 2021 May 28; in original form 2021 April 22.

## ABSTRACT

Most ULXs are believed to be powered by super-Eddington accreting neutron stars and, perhaps, black holes. Above the Eddington rate the disc is expected to thicken and to launch powerful winds through radiation pressure. Winds have been recently discovered in several ULXs. However, it is yet unclear whether the thickening of the disc or the wind variability causes the switch between the classical soft and supersoft states observed in some ULXs. In order to understand such phenomenology and the overall super-Eddington mechanism, we undertook a large (800 ks) observing campaign with XMM-*Newton* to study NGC 247 ULX-1, which shifts between a supersoft and classical soft ULX state. The new observations show unambiguous evidence of a wind in the form of emission and absorption lines from highly-ionised ionic species, with the latter indicating a mildly-relativistic outflow ( $-0.17c$ ) in line with the detections in other ULXs. Strong dipping activity is observed in the lightcurve and primarily during the brightest observations, which is typical among soft ULXs, and indicates a close relationship between the accretion rate and the appearance of the dips. The latter is likely due to a thickening of the disc scale-height and the wind as shown by a progressively increasing blueshift in the spectral lines.

**Key words:** Accretion discs – X-rays: binaries – X-rays: individual: NGC 247 ULX-1.

## 1 INTRODUCTION

There is a consensus that the majority of ultraluminous X-ray sources (ULXs) are stellar-mass compact objects (neutron stars and perhaps black holes) accreting above the critical Eddington rate (see, *e.g.*, King et al. 2001, Poutanen et al. 2007; Middleton et al. 2011, Bachetti et al. 2014, Kaaret et al. 2017). The spectral curvature in the X-ray band, with a characteristic downturn above  $\sim 5$  keV, and the presence of residuals at energies  $\lesssim 1$  keV when modelled with featureless continuum models, are two characteristic ULX features (see, *e.g.*, Soria et al. 2004, Goad et al. 2006,

Gladstone et al. 2009) that are naturally explained if the primary X-ray photons are seen through a disc wind, as expected for systems accreting in the super-Eddington regime (*e.g.*, Shakura & Sunyaev 1973, Poutanen et al. 2007). The thickness of the wind and, as a result, the “softness” of the observed ULX spectra in the  $\sim 0.1$ –20 keV band, are likely a function of two main parameters: the mass outflow rate in the wind (which is related to the accretion rate), and our viewing angle, with softer sources being observed closer to the disc plane (see, *e.g.*, Sutton et al. 2013, Middleton et al. 2015a, Pinto et al. 2017). In particular, ULXs with a power-law photon index  $\Gamma > 2$  in the  $\sim 0.3$ –5 keV band are empirically classified in a “soft ultraluminous” (SUL) state.

\* E-mail: ciro.pinto@inaf.it

### 1.1 Supersoft ultraluminous sources

Among the ULXs, a special sub-class is represented by ultraluminous supersoft sources (ULSs), also referred to as sources in the “supersoft ultraluminous” (SSUL) state (Feng et al. 2016). This state is defined by a dominant, cool blackbody component ( $T_{\text{bb}} \lesssim 140$  eV), with very weak or completely absent hard component at higher energies. Observationally, sources in the SSUL state show essentially no photons  $>1$  keV. Their bolometric luminosity is typically a few  $10^{39}$  erg  $\text{s}^{-1}$ . They should not be confused with the “classical” supersoft sources (see, *e.g.*, Krautter et al. 1996), which are usually interpreted as nuclear burning on the surface of a white dwarf. Classical supersoft sources also have blackbody spectra, but at lower luminosities ( $L_{\text{bb}} \lesssim 10^{38}$  erg  $\text{s}^{-1}$ ), and generally with a smaller bb radius:  $R_{\text{bb}} \sim 5000 - 10000$  km, consistent with a white dwarf, while SSUL spectra can have blackbody radii as large as  $10^5$  km (Urquhart & Soria 2016).

Blackbody modelling of SSUL spectra at different epochs shows that the characteristic radius is not constant, which rules out a hard surface as the origin of the thermal emission (Feng et al. 2016). It also shows a clear anti-correlation between blackbody radius and temperature, which rules out a standard accretion disc. Instead, such behaviour is consistent with emission from the photosphere of an optically-thick wind. The increase in the photospheric radius corresponds to an enhancement of the wind thickness.

The apparent non-periodic spectral variability in the SSUL state (Liu 2008) is very likely due to a thickening of the wind along our line of sight. One question we want to address is whether the short-term variations in optical depth are just stochastic variability (at a given mass accretion rate  $\dot{M}$ ) due to the clumpy nature of the wind (“weather”, see, *e.g.*, Takeuchi et al. 2013), or instead each variation is driven by a change in the underlying  $\dot{M}$  (“climate”), which then affects the wind density and launching radius.

A deep absorption edge was detected at  $\approx 1.0-1.1$  keV in several SSUL sources (*e.g.*, those in M 51, NGC 6946 and M 101: Urquhart & Soria 2016, Earnshaw & Roberts 2017). This feature clearly appears when the source softens, progressively losing all X-ray photons with energy above 1 keV. There are no strong absorption edges predicted at the observed energy of those dips. Viable solutions are blueshifted O VIII ionisation edges (871eV at rest), which was observed in novae during their supersoft phase (*e.g.*, Pinto et al. 2012), or a combination of high-ionisation Fe L or Ne IX-X absorption lines with velocities of  $\sim 0.1-0.2c$ , supporting the case for an optically-thick, mildly-relativistic wind.

### 1.2 NGC 247 ULX-1

Previous X-ray studies (see, *e.g.*, Feng et al. 2016), based on two short XMM-Newton observations, showed that NGC 247 ULX-1 switched from a supersoft state with hardly any flux above 1 keV (in 2009) to a much brighter state (in 2014) consistent with the soft end of the “standard” ULX population (*i.e.*, those with a bright hard X-ray spectral tail).

NGC 247 ULX-1 is also among the most variable ULXs. It exhibits strong dips in its X-ray lightcurve, which last several ks, and during which the flux decreases by an order of magnitude (Feng et al. 2016). Both the low and high flux spectra are characterised by strong spectral features.

**Table 1.** XMM-Newton campaign on NGC 247 ULX-1.

OBS_ID	Date	t <sub>RGS1</sub> (ks)	t <sub>RGS2</sub> (ks)	t <sub>MOS1</sub> (ks)	t <sub>MOS2</sub> (ks)	t <sub>pn</sub> (ks)
0844860101	2019-12-03	110.5	110.1	104.6	105.0	76.6
0844860201	2019-12-09	110.9	110.6	109.3	109.2	90.3
0844860301	2019-12-31	117.4	117.0	112.6	113.9	76.8
0844860401	2020-01-02	112.3	112.0	110.6	110.5	93.5
0844860501	2020-01-04	115.9	115.6	113.3	113.3	94.4
0844860601	2020-01-06	102.3	101.7	83.3	83.2	57.4
0844860701	2020-01-08	28.2	28.3	96.1	97.5	70.1
0844860801	2020-01-12	61.0	60.8	59.3	59.4	41.7
Total [ks]		758.5	756.1	789.1	792.0	600.8
Total [kcnts]		7.2	10.4	56.7	57.2	186.5

Notes: exposure times account for high background removal. Source counts are in the whole energy band for each detector.

Pinto et al. (2017) found similarities between the narrow X-ray spectral features of NGC 247 ULX-1 in the high flux state with those of NGC 55 ULX, using observations taken with the high-resolution gratings aboard XMM-Newton. Despite the short duration (33 ks) of the observations available, two remarkable absorption features at  $7.5 \text{ \AA}$  and  $16.2 \text{ \AA}$  were found along with other weaker features, which can be modelled with absorption from photoionised gas outflowing at  $\approx 0.14c$ . The observation taken in the low-flux (supersoft) state is far too short to provide any useful data. Thus, we proposed and were awarded a 800 ks deep XMM-Newton programme to characterise the properties of the outflows and the origin of the spectral residuals, and correlate them with the continuum flux variability and state changes.

This paper is the first in a series of intriguing results from our XMM-Newton campaign. Here, we focus on the search for wind signatures in the time-average spectrum, taking full advantage of the high-spectral-resolution data, and on the variability of the spectral features around 1 keV. We detail our observing campaign in Sect. 2 and present the results of our spectral analysis in Sect. 3. We discuss the results in Sect. 4, and outline some conclusions in Sect. 5.

## 2 NGC 247 XMM-NEWTON CAMPAIGN

We observed the NGC 247 galaxy between December 2019 and January 2020. The roll angle was similar throughout the whole campaign and avoided strong contamination along the dispersed grating spectra from the nearby brightest X-ray sources (see Fig. 1 and Appendix A1 for more detail). Seven observations were expected to occur but, owing to an issue with the RGS instrument that occurred during the last observation (id:0844860701), an additional final observation was taken shortly afterwards (id:0844860801) to recover the lost exposure. In Table 1, we report the detail of our observations. We performed the spectral analysis with the SPEX code (Kaastra et al. 1996), we used C-statistics (C-stat, Cash 1979) for spectral fits, which was proved to be efficient in comparing models similarly to  $\chi^2$  statistics (Kaastra 2017), and we adopted  $1-\sigma$  confidence intervals.

## 2.1 Data preparation

In this work we used data from the European Photon-Imaging Camera (EPIC), the Reflection Grating Spectrometer (RGS) and the Optical Monitor (OM) aboard XMM-Newton. The primary science was carried out with the RGS which can detect and resolve narrow spectral features. The broadband cameras (EPIC MOS 1,2 and pn) were mainly used to determine the spectral continuum and cover the hard X-ray band missed by the RGS.

### 2.1.1 EPIC cameras

We reduced the 8 new XMM-Newton observations with the Science Analysis System (SAS v18.0.0, CALDB available on March, 2020). EPIC-pn and MOS data were reduced with the EPPROC and EMPROC tasks, respectively. Following the recommended procedures, we filtered the MOS and pn event lists for bad pixels, cosmic-ray events outside the field of view, photons in the gaps (FLAG=0), and applied standard grade selections (PATTERN  $\leq 12$  for MOS and PATTERN  $\leq 4$  for pn). We corrected for contamination from high background by selecting background-quietest intervals on the lightcurves for MOS 1,2 and pn in the 10–12 keV energy band. These lightcurves were extracted in time bins of 100 s and all those with a count rate above 0.4 c/s for pn and 0.2 c/s for MOS were rejected. The MOS 1-2 and pn clean exposure times are reported in Table 1.

We extracted EPIC MOS 1-2 and pn images in the 0.3–10 keV energy range and stacked them with the EMOSAIC task (see Fig. 1). We also extracted EPIC MOS 1-2 and pn lightcurves from within a circular region of 20" radius centred on the source position ( $\alpha, \delta=00:47:04.0, -20:47:45.7$ ). We used the task EPICLCCORR, which corrects for vignetting, bad pixels, chip gaps, PSF, and quantum efficiency. The background (BKG) lightcurves were extracted from within a larger circle in a nearby region on the same chip. In order to measure the variations in the spectra hardness, we extracted EPIC-pn (for its larger effective area) lightcurves in the soft (0.3–1 keV) and hard (1–10 keV) energy bands (with 1 ks time bins to increase the signal-to-noise ratio of each bin). The PN lightcurves are shown in Fig. 2 (top-left panel) with a length above 800 ks (despite an effective clean exposure of 600ks) due to the large 1ks bin size which does not show the time gaps of high BKG lasting few 100s. The lightcurves were also glued together for displaying purposes but with vertical dotted lines separating them. The hardness ratio was defined as the fraction of hard photons with respect to the total ( $H/(H+S)$ ). The boundary energy was adopted owing to the strong spectral curvature of supersoft sources exhibited above 1 keV (see Sect. 2.1.4).

We extracted EPIC MOS 1-2 and pn spectra in the same regions used for the lightcurves. The EPIC-pn spectra of the individual observations are shown in Fig. 3. We avoided over-plotting the MOS spectra for displaying purposes.

### 2.1.2 RGS cameras

The RGS data reduction was performed with the RGSPROC pipeline. We filtered out periods affected by contamination from Solar flares by selecting background-quietest intervals in the lightcurves of the RGS 1,2 CCD 9 (*i.e.*,  $\gtrsim 1.7$  keV)

with a count rate below 0.2 c/s. As usual, Solar flares affected the RGS data on a much lower level than EPIC. The total clean exposure times are quoted in Table 1.

We extracted the 1<sup>st</sup> and 2<sup>nd</sup>-order RGS spectra in a cross-dispersion region of 0.8' width, centred on the source coordinates and the background spectra by selecting photons beyond the 98% of the source point-spread-function. The background regions do not overlap with bright sources. After inspecting the 2<sup>nd</sup>-order spectra, we decided not to use them as they were highly affected by the background. We stacked the 1<sup>st</sup>-order RGS 1 and 2 spectra from all observations with RGS COMBINE and the EPIC-pn, MOS 1 and MOS 2 spectra, using EPIC SPEC COMBINE. The stacking provided 4 time-averaged high signal-to-noise spectra for RGS, MOS 1, MOS 2, and pn detectors.

All XMM-Newton spectra were grouped in channels of at least 1/3 of the spectral resolution, for optimal binning and to avoid over-sampling, and at least 25 counts per bin, using SAS task SPEC GROUP. This has also the advantage to smooth the background spectra in the energy range with low statistics, avoiding narrow spurious features introduced by the background subtraction. This also enabled us to check our results with the  $\chi^2$  statistics. The stacked spectra have many counts with the binning affecting only the spectral range at the rather low and high energies (outside the 0.6-1.7 keV RGS band and above 4 keV in EPIC spectra), where line detection is not crucial. We found no significant effect onto our line or continuum modelling by decreasing the binning to just 1/3 of the spectral resolution.

### 2.1.3 Optical Monitor

We used OM data to search for a possible optical/UV counterpart to NGC 247 ULX-1. To increase the signal-to-noise ratio we stacked all the internally aligned full-frame sky images per filter and per observation, using the SAS tool OM MOSAIC. Each observation contains at least one image in one of these filters: V, UVW1, UM2 and UVW2 and the final total exposures corresponded to 105 ks, 105 ks, 115 ks and 220 ks, respectively. We ran the OMDetect task on these stacked images with a limit on the detection threshold of  $2\sigma$ . At the position of the ULX (Section 2.1.1), no source was detected in any of the filters. This is unsurprising since the ULX region is very close to a bright association of OB stars, which makes such a detection challenging. To derive an upper limit for the ULX emission in these bands, we computed the total background rate for a circular region of 6" around the position of the ULX. This provided  $3\sigma$  upper limits for the ULX flux, which are comparable to previous measurements obtained by Feng et al. (2016) using deep observations with Hubble Space Telescope (HST, UV-optical fluxes  $\sim 10^{-14}$  erg s<sup>-1</sup> cm<sup>-2</sup>). In the far-UV the OM flux upper limits are slightly below the HST detections, suggesting long-term flux variability and that a substantial fraction of the UV flux originates within the accretion disc rather than the stellar companion (see Fig. A3, top panel).

A final OM image obtained by stacking the data from all the filters of all the observations is shown in Fig. 1, bottom panel, where the bright association of OB stars can be seen on the right side of the X-ray source centroid.

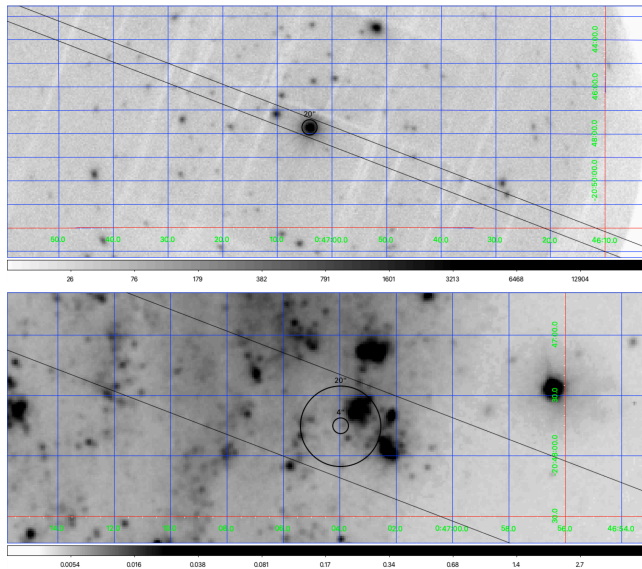


**Figure 1.** XMM-Newton image of the NGC 247 field obtained by combining all the data available for EPIC-pn and MOS1,2 zooming onto the ULX-1 region (top panel). The black strip and circle indicate the RGS and EPIC extraction regions, respectively. The bottom panel shows the time-averaged image obtained by stacking all the data from the Optical Monitor. A small circle with 4'' radius shows the X-ray source centroid.

#### 2.1.4 Data investigation

The XMM-Newton 0.3–10 keV lightcurve shows a strong dipping behaviour with the source flux approaching zero  $c/s$  during time interval of less than 15 ks, as found by Feng et al. (2016), see Fig. 2 (top-left panel). The dips have variable duration, with the shortest ones being of a few hundred seconds, which was estimated extracting finer lightcurves (D’Ài et al. in prep). During the dips, the flux drops by an order of magnitude and then returns to the previous level, which makes it difficult to believe it is due to an intrinsic flux change rather than to a temporary obscuration phenomenon. This behaviour causes the multiple peaks present in the histogram of the count rates (Fig. 2, right panel), which disagree with a single-peaked log-normal trend.

The hardness ratio decreases during the dips (Fig. 2, bottom-left panel), which is very similar to the soft source NGC 55 ULX-1 (Pinto et al. 2017). This was interpreted as evidence of temporary obscuration of the inner hot regions from a clumpy disc wind (e.g., Stobbart et al. 2006).

The lightcurve also shows that NGC 247 ULX-1 undergoes a long-term flux variability with observations 4-to-6 exhibiting significantly higher fluxes. Importantly, the frequency of the dips was higher during these observations.

In order to evaluate the source variability during each observation, we calculated the fractional excess variance of the EPIC-pn lightcurve of each observation and the root-mean-square (RMS), following standard formulae (see, e.g., Nandra et al. 1997, Vaughan et al. 2003, and Allevato et al. 2013). We adopted time bins of 1 ks and, as time length, the duration of each exposure ( $\sim 100$  ks, with the exception of obsid:0844860801). The computed RMS values are reported in Table A1 and range from about 10 to 55 %.

The EPIC spectra of the individual observations in Fig. 3 show a variability pattern that is common to ULXs,

with the harder band ( $> 1$  keV) exhibiting the largest variation (see, e.g., Middleton et al. 2015a, Brightman et al. 2016, and Walton et al. 2018c). A thorough analysis of the variability pattern involving a careful sampling of time interval with similar flux and hardness ratio, and the study of the power density spectra, will be done in two separate papers (D’Ài et al. in prep, Alston et al. 2021).

### 3 SPECTRAL ANALYSIS

In this section we present the spectral analysis of NGC 247 ULX-1. We first show the time evolution of the main spectral residuals around 1 keV through the modelling of the spectral continuum in EPIC spectra from different observations (see Sect. 3.1). Then we will perform a thorough analysis of the high-statistics, time-averaged, stacked spectrum in order to identify the lines in the RGS (Sect. 3.2 and 3.3), to build the spectral energy distribution (SED), and to use physical plasma models for the wind detection and modelling (Sect. 3.4 and 3.5). The final best-fit models are shown in Sect. 3.6 and the statistical significance of our findings in Sect. A5.

ULX spectra require up to three components to obtain a satisfactory description of the spectral continuum. Two blackbody-like components are often used to model the soft (0.3–1 keV) and hard (1–10 keV) X-ray energy bands (see, e.g., Stobbart et al. 2006, Pintore et al. 2015). The availability of high-statistics spectra and broadband data reveals the presence of a third harder component, which dominates the continuum above 10 keV (see, e.g., Walton et al. 2018a). In the framework of super-Eddington accretion, the cooler, soft, component corresponds to the X-ray emission of the wind and the disc around the spherisation radius. The hard component refers to the inner accretion flow. The hard ( $> 10$  keV) tail is either due to Compton scattering in the innermost regions or from an accretion column (see, e.g., Middleton et al. 2015a). The two hard components, especially the hard tail, are weak in supersoft ULXs.

#### 3.1 Time evolution of the $\sim 1$ keV residuals

For the modelling of EPIC spectra of individual observations we adopted a simple continuum model consisting of two blackbody (*bb*) components, which is often used as a proxy for more complex models (see, e.g., Walton et al. 2014, Pinto et al. 2017, Koliopanos et al. 2017, and Gúrpide et al. 2021). We did not model the hard tail in the individual spectra because it is so weak that any model would be highly unconstrained, but for the time-averaged SED modelling we took it into account (see Sect. 3.2). The emission components are corrected for absorption by the Galactic interstellar medium and the circumstellar medium near the ULX using the *hot* model in SPEX with a low temperature ( $kT = 0.2$  eV, e.g. Pinto et al. 2013), at which the gas is neutral. In the spectral fits, we coupled the column density of the *hot* model across all observations as it is unlikely that the amount of neutral gas along our line of sight towards the ULX would change on time scales of a few days. In some Galactic X-ray binaries (XRB) variable obscuration was found, but it is not clear whether these findings are related to ionised gas (i.e. winds) or uncertainties in the continuum rather than neutral gas (see, e.g., Miller et al. 2009, Walton et al. 2017).

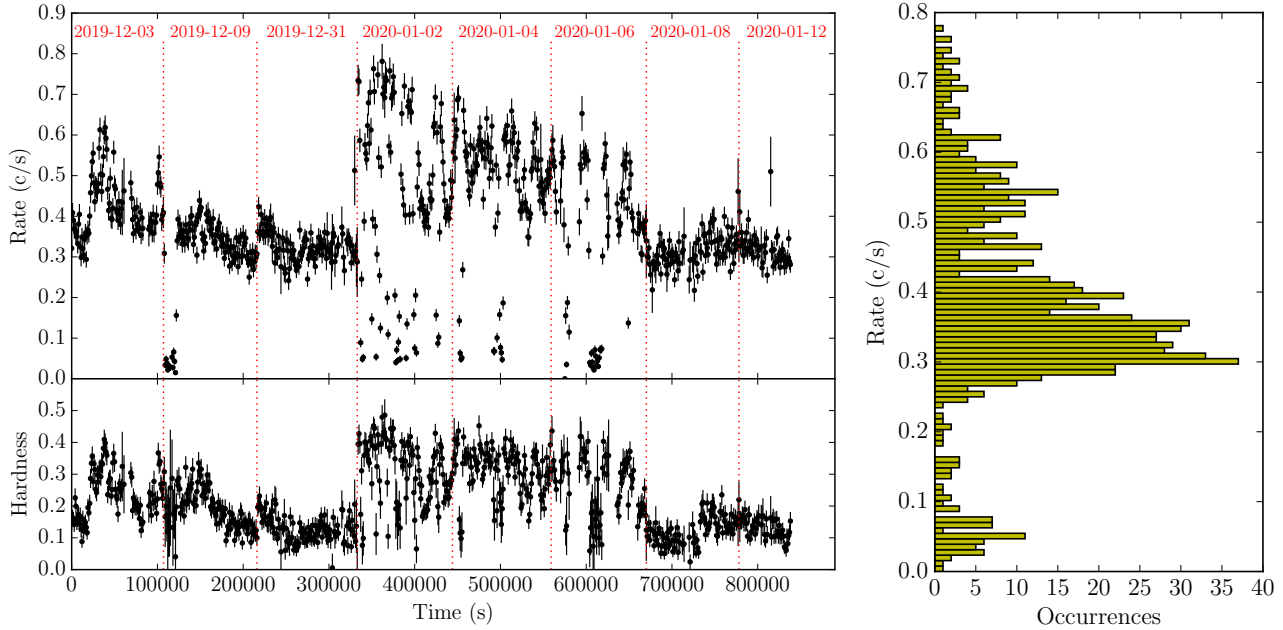


**Figure 2.** Top left panel: cumulated XMM-Newton (0.3–10 keV) pn lightcurve of NGC 247 ULX-1 with the individual observations separated by vertical dotted lines. Time bin size is 1 ks. Obsid 3-to-7 are separated by 20-60 ks each. Bottom left panel: hardness ratio ( $H/(H+S)$ ) estimated from the lightcurves in the soft (0.3–1 keV) and hard (1–10 keV) X-ray bands. Right panel: count rate histogram.

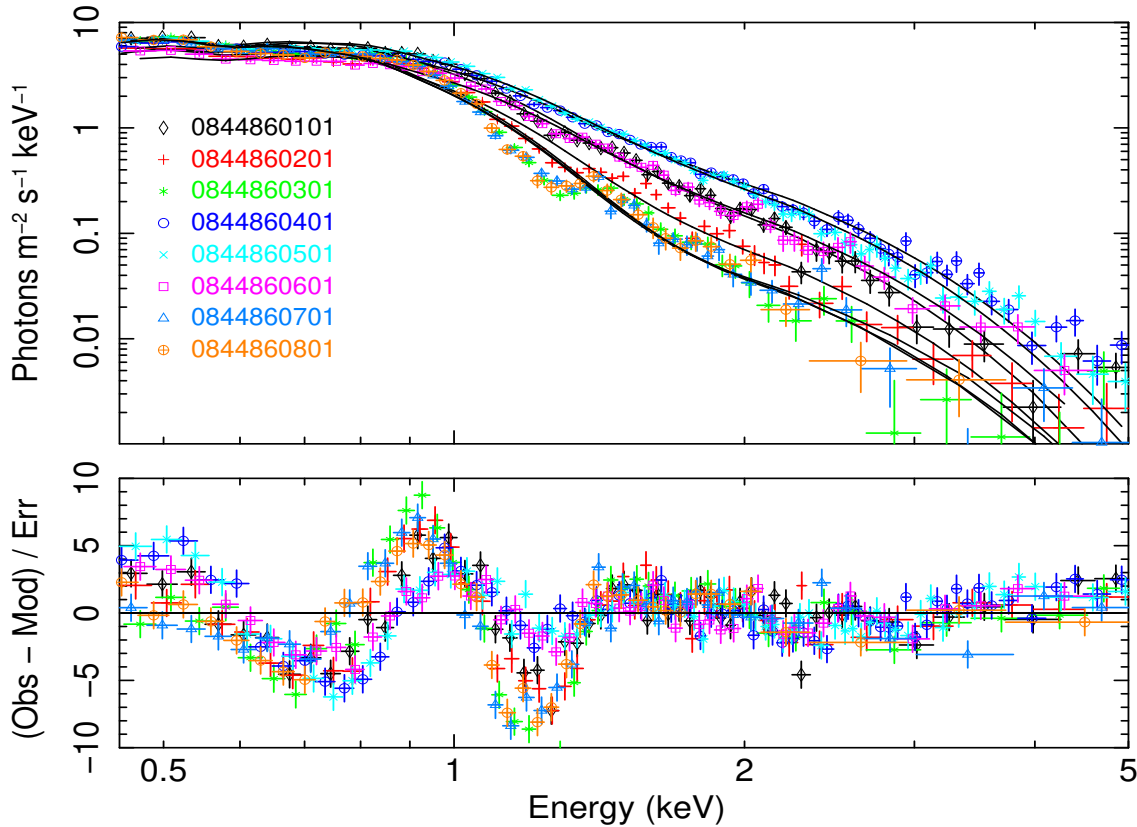


**Figure 3.** XMM-Newton EPIC-pn spectra of NGC 247 ULX-1. The top panel shows the pn spectra of the individual observations with overlaid the 2-blackbody continuum models. The bottom panel shows the corresponding residuals. Both the emission feature below 1 keV and the absorption feature above 1 keV vary in centroid and strength according to the continuum flux and shape. This is qualitatively similar to the intermediate-hard source NGC 1313 ULX-1 and the soft source NGC 55 ULX-1 (Middleton et al. 2015b; Pinto et al. 2017).

We simultaneously applied the *hot (bb + bb)* continuum model to the EPIC MOS 1,2 and pn spectra of all eight observations. The results are shown in Fig. 3 and Table A1. We obtained an average column density of  $N_{\text{H}} = (3.4 \pm 0.1) \times 10^{21} \text{cm}^{-2}$ . This phenomenological model provides a good description of the broadband spectra, but the *C*-statistics are high when compared to the corresponding degrees of freedom ( $C_{\nu} \sim 3-9$ ) due to the well-known strong and sharp residuals in the form of absorption and emission features around 1 keV (see Fig. 3).

It is possible to understand the nature of the residuals by tracking their temporal evolution from one observation to another. In Middleton et al. (2015b) and Pinto et al. (2017), the three main spectral features observed around 1 keV in the spectra of NGC 1313 ULX-1 and NGC 55 ULX-1 were modelled with a positive (emission) and two negative Gaussians (absorption) lines. The availability of deeper observations allow us to fit the three Gaussian components independently, but we fixed the line broadening to zero km/s (*i.e.* only instrumental broadening) in order to minimise the degeneracy that can be produced by the low spectral resolution of EPIC. We chose three Gaussian lines as previous work on high-resolution RGS data identified Fe/Ne emission lines at 1 keV, O VIII absorption lines around 0.7–0.8 keV, and Fe/Ne absorption lines above 1 keV (Pinto et al. 2016). Using only one or two Gaussian lines always resulted in significantly worse fits during alternative tests.

The *hot (bb + bb) + (gaus + gaus + gaus)* spectral model improves the fits for all observations with respect to the *hot (bb + bb)* model. In Table A1, we report the best-fitting parameters for each observation. The reduced C-stat are still rather high due to additional residuals that require more complex and physical models. Moreover there is evidence of a weak, broad, hard tail in all spectra above 3 keV, which cannot be explained with atomic lines (Fig. 3).

In Fig. 4, we compare the energy centroids (left panel) and the fluxes (right panel) as measured for the three Gaussian lines in the EPIC spectra of the eight observations. The point size was coded according to the value of their RMS estimate in Sect. 2.1.4. Both the energies and fluxes of the Gaussians lines vary with the time, showing a higher blueshift and lower flux (in absolute value) during the dipping observations with enhanced variability.

### 3.2 Time-averaged continuum: spectral modelling

The RGS spectra of the individual observations do not provide statistics sufficient to detect and resolve the spectral residuals with high significance. The 750 ks RGS 1+2 stacked spectrum instead has a much higher quality and enables line detection, despite the low source flux.

We simultaneously fitted the time-averaged stacked EPIC MOS 1,2 and pn, and the RGS spectra using the absorbed double-blackbody continuum model (*hot (bb + bb)*) adopted for the spectra of the individual observations. The hard tail above 3 keV is more evident in the stacked data and, therefore, we accounted for it using a third, hotter ( $kT \sim 1$  keV), blackbody as to mimic additional hard X-ray photons down-scattered through the disc photosphere (and/or the wind). The three-blackbody model brings the C-stat from 4671 down to 4488 for four additional degrees of freedom. In all fits the parameters of the blackbody and

**Table 2.** Time-averaged EPIC+RGS spectral fits.

Parameter	Units	<i>hot (bb + bb)</i>	<i>hot (bb + bb + bb)</i>
<i>Area, bb</i> <sub>1</sub>	10 <sup>19</sup> cm <sup>2</sup>	3.4 ± 0.3	4.5 ± 0.3
<i>Area, bb</i> <sub>2</sub>	10 <sup>16</sup> cm <sup>2</sup>	1.0 ± 0.1	1.7 ± 0.2
<i>Area, bb</i> <sub>3</sub>	10 <sup>13</sup> cm <sup>2</sup>	–	1.7 ± 0.5
<i>kT, bb</i> <sub>1</sub>	keV	0.120 ± 0.001	0.116 ± 0.001
<i>kT, bb</i> <sub>2</sub>	keV	0.382 ± 0.003	0.342 ± 0.005
<i>kT, bb</i> <sub>3</sub>	keV	–	1.05 ± 0.07
$L_{X,tot}$	10 <sup>39</sup> erg/s	5.3 ± 0.5	6.2 ± 0.5
$N_{\text{H}}$	10 <sup>21</sup> cm <sup>-2</sup>	3.64 ± 0.05	3.84 ± 0.05
C-stat/d.o.f.		4671/1136	4488/1132

$L_{X(0.3-10 \text{ keV})}$  luminosities are calculated assuming a distance of 3.3 Mpc and are corrected for absorption (or de-absorbed). The best-fit three-blackbody model and the spectra are shown in Fig. 6. Both models are shown in the SED modelling in Fig. A3.

the ISM absorber were coupled among the EPIC and RGS models. We left the overall normalisations of the MOS 1,2 and RGS models free to vary with respect to pn in order to account for the typical 5-10% cross-calibration uncertainties among their effective areas. Details on the spectral fits for both models are reported in Table 2 and Fig. 5. In order to avoid a crowded plot, we did not include the more noisy RGS spectrum in this plot, while it is shown later in Figs. 6 and 7 where the EPIC data below 1.77 keV was ignored.

The blackbody models used so far are the simplest available and allowed us to constrain the parameters. We tested various combination of two-components models to possibly improve the description of the spectral continuum before accounting for narrow features. These consisted of the cool blackbody component plus either a disc blackbody (*ddb*) or a disc blackbody modified by coherent Compton scattering (*mhb*) or Comptonisation (*comt*). These did not provide improvements with respect to the three blackbody model. Similar results were provided by more complex three-component continuum models which anyway over-fit the data and lead to degeneracy among model parameters due to the weak hard (> 1 keV) continuum. Alternatively, one could use the common blackbody plus powerlaw emission model. However, the powerlaw would be very steep with a consequent unphysical divergence in the soft band, which would badly affect the ionisation balance calculation (see, *e.g.*, Pinto et al. 2020a).

### 3.3 Time-averaged continuum: Gaussian line scan

In Fig. 6, we show the stacked RGS and EPIC spectra, indicating the dominant H-/He-like transitions of the X-ray band often found in the spectra of X-ray binaries. A zoom over the RGS spectrum with ad-hoc linear Y-axis can be found in Fig. 7. The RGS exhibits substantial residuals at the same energies as the EPIC residuals but resolves them in a structure of lines, although the former have lower count rates. Strong emission-like features appear near the transition energies of the most relevant neon K and iron L lines. Additional features may be related to N VII and O VII-VIII, although the background starts to be important in the RGS below 0.6 keV. Some possible absorption-like features are indicated with vertical dotted lines. The very good agreement between the positions of the RGS, MOS 1,2 and pn residuals rules out instrumental dominant features.

Following the approach used in Pinto et al. (2016), we

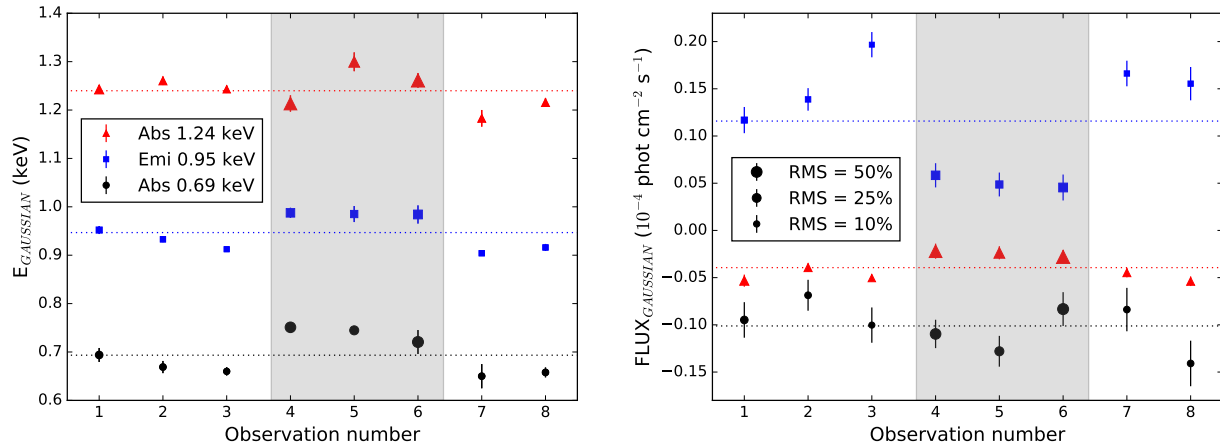


**Figure 4.** Evolution of the XMM-Newton EPIC spectral residuals around 1 keV. The left and the right panels show the energy centroid and normalisation of the Gaussian lines used to fit the three main (unresolved) spectral residuals, respectively. The shaded grey areas highlight the observations of high spectral variability and dipping. ‘Abs’ and ‘Emi’ refer to absorption and emission features, respectively.

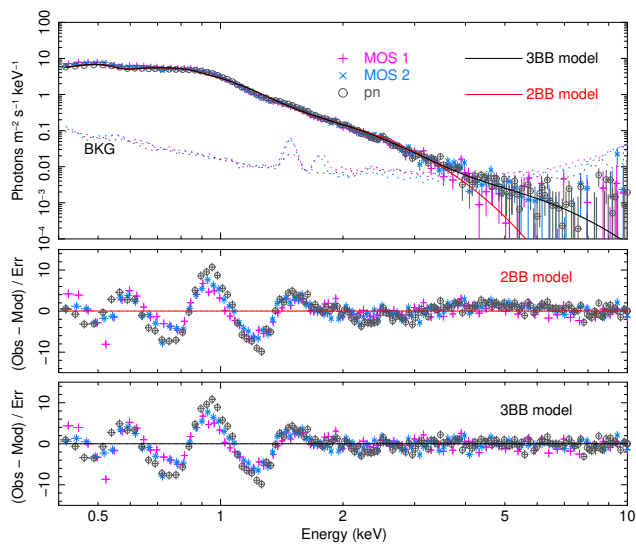


**Figure 5.** Time-averaged XMM-Newton EPIC-pn and MOS 1,2 spectra. Overlaid are two alternative continuum models consisting of two (red line) and three (black line) blackbody components.

searched for narrow spectral features by scanning the spectra with Gaussian lines. We adopted a logarithmic grid of 1000 points with energies between 0.3 (41 Å) and 10 keV (1.24 Å). This choice provided a spacing that is comparable to the RGS and EPIC resolving power in the energy range we are investigating ( $R_{\text{RGS}} \sim 100 - 500$  and  $R_{\text{EPIC}} \sim 20 - 60$ ). We tested line widths ( $\sigma_G = \text{FWHM}/2.355$ ) of 100, 250, 500 and 1000 km/s, which are comparable to the RGS resolution. At each energy we recorded the  $\Delta C$  improvement to the best-fit continuum model and expressed the significance as the square root of the  $\Delta C$ . This provides the maximum significance for each line (as it neglects the number of trials). We multiplied  $\sqrt{\Delta C}$  by the sign of the Gaussian normalisation to distinguish between emission and absorption lines.

In Fig. 8 we show the results of the line scan obtained for the time-averaged stacked RGS+EPIC spectra using the three-blackbody continuum model. We performed the line scan in two ways: the first run using all RGS data (0.3–2

keV) and EPIC data (0.3–10 keV) and the second one ignoring the EPIC data between 0.33 and 1.77 keV, where the RGS effective area is well calibrated. When fitting only RGS in the 0.33–1.77 keV energy band we always fixed the temperatures of the blackbody components to the best-fit values obtained using the EPIC data in the whole 0.3–10 keV. This is due to the low count rate of the RGS spectra that limited our capability to constrain the overall continuum level and shape (see Pinto et al. 2020b).

The line scan of the EPIC + RGS spectra data picked out the strong emission-like features near 1 keV and other two around 0.6 and 1.5 keV. Broad absorption features were also found around 0.7 and 1.2–1.3 keV as previously done in the spectrum of each observation (see Fig. 4 and Table A1).

Owing to the low spectral resolution and high count rate of EPIC, the features appear very broad ( $\sim 0.1$  keV) in the EPIC+RGS Gaussian scan preventing us from identifying them. This becomes easier above 2 keV due to the increasingly higher EPIC spectral resolution. The Gaussian scan performed using only RGS between 0.33 and 1.77 keV resolved the features into a forest of lines. Multiple lines are responsible for the 1 keV emission-like and the 1.2–1.3 keV absorption-like features. Interestingly, most absorption features are consistent with some Lyman  $\alpha$  transitions also seen in emission, if we assume a systemic blueshifted absorption of about  $0.17c$  (see vertical ticks in Fig. 8). The 0.6 keV features might either be interpreted as a blueshifted O VII  $\alpha$  triplet or redshifted O VII  $\beta$  + O VIII Ly  $\alpha$  emission lines. The emission lines found between 0.9–1 keV are most likely from Ne IX-X and Fe XVIII-XXIV ions. Alternative interpretations correspond to different velocities of the X-ray emitting (and absorbing) plasmas. The use of physical models is necessary to distinguish among the several interpretations. The most simple physical models involve the adoption of plasma in either collisionally-ionisation equilibrium (CIE) or photoionisation equilibrium (PIE).

The single-trial line significance (“ $\sigma_{ST}$ ”) of the individual strongest features is around  $5\sigma$ , which of course is smaller if we take into account the look-elsewhere effect. However, plasma models are able to model multiple lines, combining their individual  $\Delta C$  improvements to the best-fit continuum, and boost the overall significance (see below).

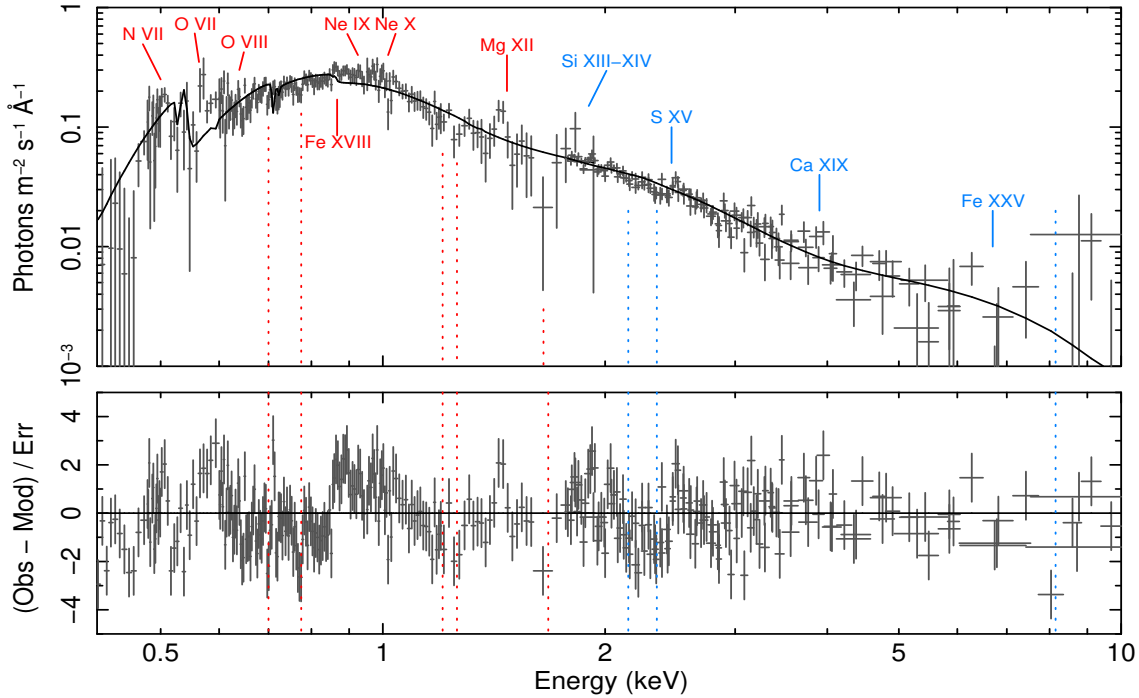


**Figure 6.** Top panel: time-averaged XMM-Newton RGS (0.33–2 keV) and EPIC MOS 1,2-pn (1.77–10 keV) spectra. Overlaid is the baseline 3-blackbody continuum model (solid black line, see Table 2). The bottom panel shows the residuals calculated with respect to the continuum model. The rest-frame energies of the most common strong transitions in the X-ray band (red for RGS band and blue for EPIC) and the absorption features (dotted lines) are also shown. All spectra were rebinned for displaying purposes.

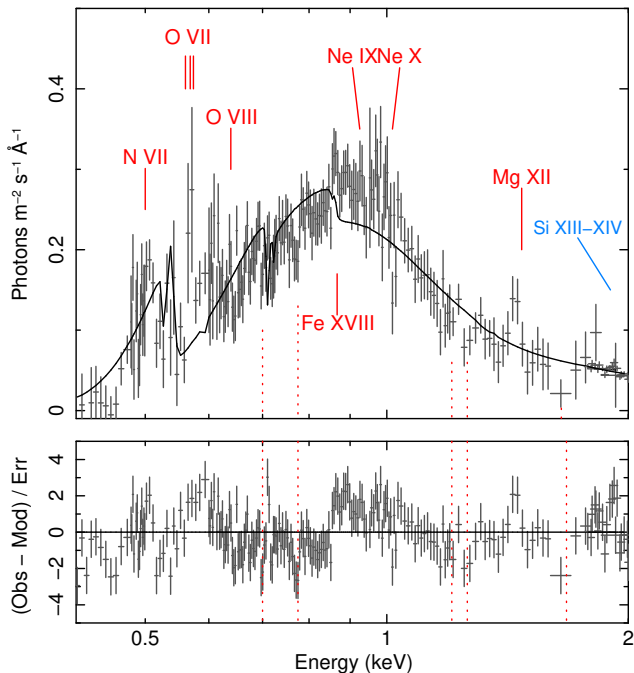


**Figure 7.** Time-averaged XMM-Newton RGS (0.33–2 keV) and EPIC-pn (1.77–10 keV) spectra. Overlaid is the baseline continuum model. This is a zoom of Fig. 6 onto the RGS data.

### 3.4 Collisional-ionisation jet modelling

Pinto et al. (2020b) performed automated scan models using either CIE or PIE plasmas. This technique prevents the fits from getting stuck in local minima, although is computationally expensive (lasting a few hours on one CPU).

#### 3.4.1 Collisionally-ionised emitting gas

Following Kosec et al. (2018b) and Pinto et al. (2020b), we performed a multidimensional automated scan with an emission model that assumes collisional ionisation equilibrium (*cie* model in `SPEX`). We adopted a logarithmic grid of temperatures between 0.1 and 5 keV (50 points), and line-of-sight velocities,  $v_{\text{LOS}}$ , between  $-0.3c$  (blueshifted jet) and  $+0.3c$  (redshifted jet, with steps of 500 km/s). We tested several values of velocity dispersion (from 100 to 10000 km/s), finding comparable results as already shown by the Gaussian line scan in Fig. 8, with the best fit achieved at  $v_{\text{RMS}} \sim 3000$  km/s. Abundances were chosen to be Solar (to limit the computing time) and the emission measure  $EM = n_e n_H V$  was the only free parameter of the CIE in the spectral fit.

We applied the automated routine scanning CIE models onto the NGC 247 ULX-1 time-averaged RGS (0.33–2 keV) and EPIC MOS 1,2-pn (1.77–10 keV) spectra. We adopted the three-blackbody continuum model shown in Sect. 3.2 and Table 2 (see also black line in Fig. 6). The results are shown in Fig. 9 (left panel). The best-fit corresponds to a large improvement with respect to the continuum model ( $\Delta C = 82$ , for 4 additional degrees of freedom) and was achieved for a CIE temperature of 0.9 keV and a small blueshift of around 6500 km/s ( $\sim 0.022c$ ). These results were driven by the strong lines that can be seen in the RGS spectrum  $\lesssim 1$  keV in Fig. 8 (bottom two panels).

We have checked our method by testing an identical CIE scan on the well-known Galactic X-ray source SS 433. This source is not ultraluminous in the X-ray band due to obscuration of the accretion disk from local circumstellar gas, but exhibits a persistent and bright ( $10^{40}$  erg/s) radio jet, which is powering a luminous optical super-bubble (Brinkmann

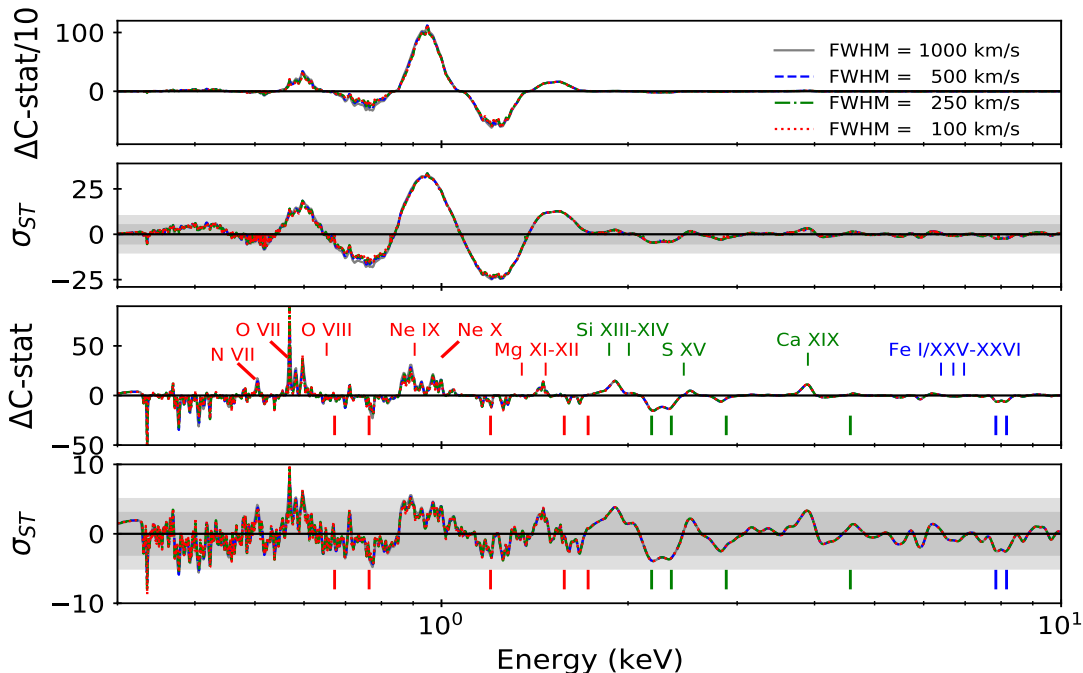


**Figure 8.** Gaussian line scan performed on the time-averaged XMM-*Newton* EPIC and RGS spectra of NGC 247 ULX-1. The top panels show the case when the EPIC spectra are used throughout the whole 0.3–10 keV band, while the bottom two panels show the results obtained with RGS between 0.33–2 keV and EPIC-pn from 1.77–10 keV (see also Fig. 6). The results for four different line widths are shown. No remarkable difference is observed among the adopted widths. The single-trial line significance (“ $\sigma_{ST}$ ”) is calculated as square root of the  $\Delta C$  times the sign of the Gaussian normalisation (positive/negative for emission/absorption lines). Labels are red for RGS, green for strong EPIC features and blue for the faint Fe K. The grey shaded areas show the 3 and 5  $\sigma_{ST}$  limits for individual lines.

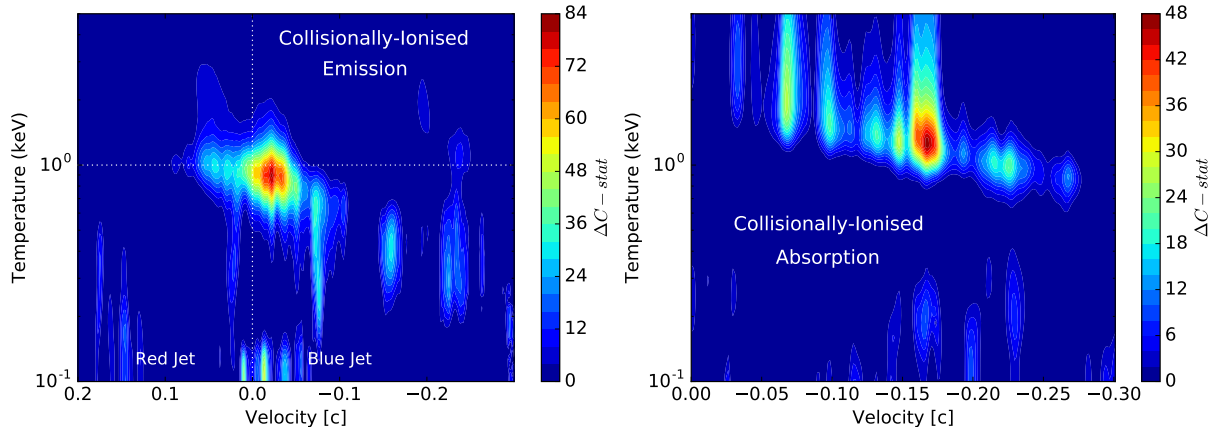


**Figure 9.** Multi-dimensional scans of collisional-ionisation emission (left panel) and absorption models (right panel) for NGC 247 ULX-1 time-averaged EPIC+RGS spectra. The X-axis shows the line-of-sight velocity (negative means blueshift, *i.e.* motion towards the observer). The color is coded according to the  $\Delta C$  fit improvement to the spectral continuum model.

et al. 1996; Fabrika 2004; Medvedev et al. 2020). SS 433 is therefore considered to be viewed edge-on. Were it observed face-on, it would likely appear as a ULX (Begelman et al. 2006; Poutanen et al. 2007; Middleton et al. 2018). SS 433 also shows a relativistic jet in the form of blueshifted lines from multi-temperature plasma in collisional-ionisation equilibrium (Marshall et al. 2002). The results obtained for SS 433 are very similar to NGC 247 ULX-1 and in agreement with Marshall et al. (2013) and Medvedev et al. (2018), which supports our method (see Appendix A3).

### 3.4.2 Collisionally-ionised absorbing gas

It is uncommon to adopt absorption models of gas in collisional-ionisation equilibrium in accreting objects as 1) it is difficult to distinguish between photoionisation and collisional ionisation on the sole basis of the dominant resonant absorption lines and 2) we hardly expect any jet to absorb the X-ray source continuum along our line of sight. However, we cannot exclude that shocks are produced by interaction between the ULX wind and the stellar companion or the surrounding bubble (or within the wind itself). Therefore, we also performed a model scan with the *hot* model in *SPEX*, which works just like *cie* but assumes absorbing gas.

In Fig. 9 (right panel) we show the results using the *hot* model over the same  $kT$  range used for the emitting gas, adopting a velocity dispersion of 500 km/s and line-of-sight velocities,  $v_{\text{LOS}}$ , ranging between  $-0.3c$  and zero, *i.e.* only Doppler blueshifts or outflows rather than inflows. The best-fit solution is obtained for a  $-0.17c$  blueshifted with a remarkable  $\Delta C = 48$  as suggested by the detection of several negative Gaussians blueshifted by similar values in Fig. 8.

### 3.5 Photoionisation wind modelling

The emission and absorption lines can be produced by winds rather than by jets as expected in the case of super-Eddington accretion discs and, therefore, in ULXs. Accurate photoionisation models require knowledge of the radiation field, *i.e.* the SED from optical to hard X-ray energies.

#### 3.5.1 SED and photoionisation balance

Following Pinto et al. (2020a,b), we built the time-averaged SED of NGC 247 ULX-1 using data from the XMM-Newton campaign and archival HST observations (as taken from Feng et al. 2016). For issues regarding the non simultaneity of HST and XMM observations, see Appendix A4. For the X-ray band (0.3–10 keV or  $\sim 10^{16-18}$  Hz) we used the best-fit three-blackbody continuum model, estimated in Sect. 3.2, Fig. 5 and Table 2. As shown in Sect. 2.1.3, the OM filters were not sensitive enough to detect the optical counterpart, but their flux upper limits in the optical and UV energy bands are however comparable to the HST measurements (see Fig. A3 top panel). We therefore modelled the optical/UV portion of the SED with the two-blackbody model of Feng et al. (2016), which together with the three-blackbody X-ray model formed our five-blackbody SED model.

We can describe the photoionisation equilibrium with the ionisation parameter,  $\xi$ , defined as  $\xi = L_{\text{ion}}/(n_{\text{H}} R^2)$  (see, *e.g.*, Tarter et al. 1969), where  $L_{\text{ion}}$  is the ionising luminosity (measured between 13.6 eV and 13.6 keV),  $n_{\text{H}}$  the hydrogen volume density and  $R$  the distance from the ionising source. The ionisation balance was calculating with the SPEX *pion* model, which calculates the transmission and the emission of a thin slab of photoionised gas, self-consistently.

Following Pinto et al. (2020b), we also computed the stability (or  $S$ ) curve, which is the relationship between the temperature (or the ionisation parameter) and the ratio between the radiation and the thermal pressure, which can be expressed as  $\Xi = F/(n_{\text{H}}ckT) = 19222\xi/T$  (Krolik et al. 1981). The stability curve is shown in Fig. A3 (bottom panel). The branches of the  $S$  curve with a negative gradient are characterised by thermally unstable gas. In this work, we assumed that the wind is seeing the same SED that we observe and, therefore, adopted the five-blackbody model SED and ionisation balance. Systematic effects from the SED choice are discussed in Sect. 4 and Appendix A4.

#### 3.5.2 Photoionised emitting gas

Once the SED and the ionisation balance were computed, we scanned the time-average EPIC+RGS spectra with the SPEX *pion* model with the same multi-dimensional routine used for the *cie* model in Sect. 3.4.1, and a similar parameter

space. We adopted a logarithmic grid of ionisation parameters ( $\log \xi$  [erg/s cm] between 0 and 6 with 0.1 steps). The only free parameter for the *pion* is the column density,  $N_{\text{H}}$ .

Unlike NGC 1313 ULX-1, the RGS spectrum of NGC 247 ULX-1 does not exhibit well resolved emission line triplets. This is perhaps due to the longer integration time required and the variability of the line centroid (see Fig. 4), which could wash out the triplets when stacking all the spectra. Additionally, the crucial O VII complex is affected by the background noise. The lack of He-like triplets means that the volume density and the luminosity of the photoionised gas are degenerate. Fitting both parameters results in poor constraints and much higher computation time. We therefore chose not to fit the volume density and adopted  $n_{\text{H}} = 10^{10}$  cm $^{-3}$ , which is a lower limit found for NGC 1313 ULX-1 (Pinto et al. 2020b). This would only slightly affect the overall flux and column density of the *pion* component.

The *pion* covering fraction is set to zero (*i.e.* *pion* only produces emission lines) and the solid angle  $\Omega = 4\pi$ . Fitting additional parameters such as  $\Omega$  might provide even better fits but would significantly increase the computing time, without altering the velocity and ionisation parameters.

In Fig. 10 (left panel) we show the results obtained using a *pion* line width of 1000 km/s. The confidence level (CL) is expressed in  $\sigma$ , which is constrained using Monte Carlo simulations (see Sect. A5). A peak ( $\Delta C = 77$ ) corresponding to a solution of blueshift emission is seen around 0.02 – 0.03c in agreement with the CIE model scans (see Sect. 3.4 and Fig. 9). However, the different ionisation balance and types of emission lines in the photoionisation equilibrium detected another, stronger ( $\Delta C = 102$ ), peak corresponding to a redshift of  $\sim +0.05c$ .

#### 3.5.3 Photoionised absorbing gas

In principle, we could just use *pion* for both emission and absorption. However, this model re-calculates the ionisation balance at every iteration and therefore is computationally expensive. Therefore, for the absorbing gas we chose to use the faster *xabs* model, which is optimized for absorption and adopts the pre-calculated ionisation balance (see Sect. 3.5.1).

The *xabs* model shares several parameters with *pion* except the opening angle of the line emission which is zero since no emission is present in this model. We adopted a covering fraction equal to unity in order to avoid degeneracy and reduce the computing time. We calculated the grid of photoionised *xabs* models in the same way as the *pion* models, but assuming line-of-sight velocities,  $v_{\text{LOS}}$ , ranging between  $-0.3c$  and zero, *i.e.* only Doppler blueshifts as for the CIE *hot* absorption models in Sect. 3.4.2.

In Fig. 10 (right panel) we show the probability distributions from scans of the RGS and EPIC spectra with  $v_{\text{RMS}} = 1000$  km/s. As expected, our code confirmed the  $v = -0.17c$  solution ( $\Delta C = 46$ ).

### 3.6 Final fits with physical plasma models

In order to check the inter-dependence of the emitting and absorbing plasma components and to test for any variations in the values of their parameters we performed two more fits of the RGS and EPIC data (with EPIC still excluded

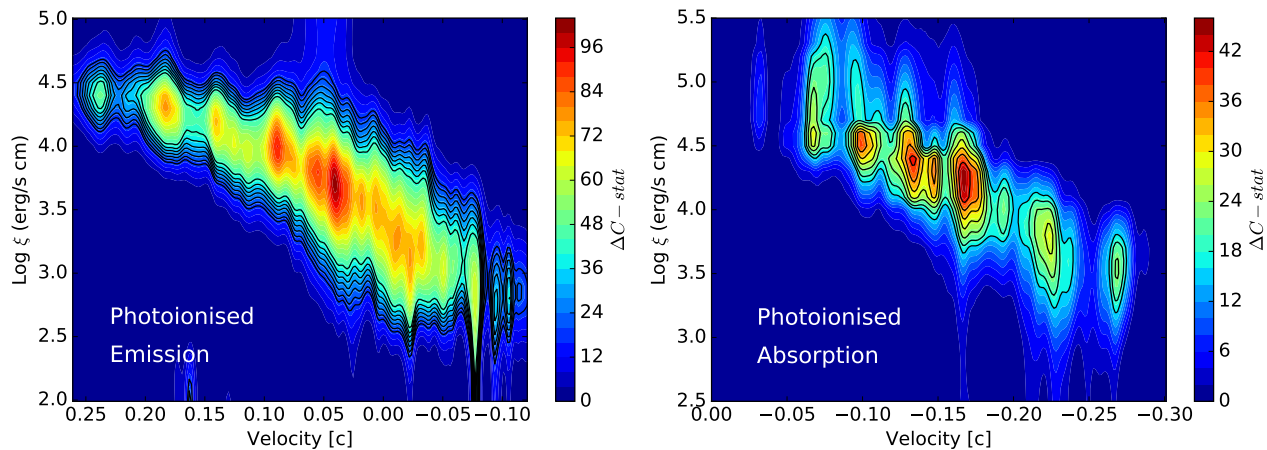


**Figure 10.** Scans of photoionisation emission (left) and absorption (right) models for the time-averaged EPIC and RGS spectra. Labels are same as in Fig. 9. The black contours refer to the (2.0, 2.5, ... 4.5, 5.0)  $\sigma$  confidence levels estimated by Monte Carlo simulations.

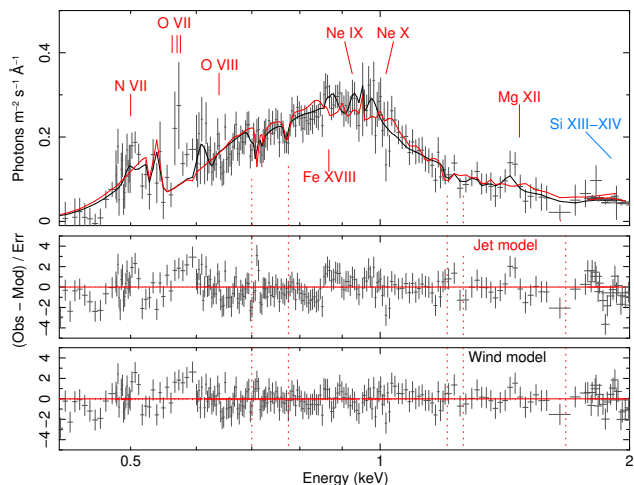


**Figure 11.** Time-averaged XMM-Newton RGS (0.33–2 keV) and EPIC-pn (1.77–10 keV) spectra. Overlaid are two alternative models (jet - CIE, red line and the wind - PIE, black line). The spectra were regrouped and the plot zoomed onto the RGS data and the 0.4–2 keV energy band for displaying purposes.

between 0.33–1.77 keV) adding onto the 3-blackbody continuum two alternative plasma models. The first one was a wind model that used the *pion* in emission and the *xabs* in absorption. The second model was an approximation of jets and shocks in the form of *cie* component in emission and *hot* component in absorption. The results for the two models are shown in Table 3 and Fig. 11 (zoomed onto the RGS). The absorption components provided very similar results, especially for the column densities and the line-of-sight velocities. As previously noted, the emission components show some differences. The results are discussed in Sect. 4.

The temperatures of the three blackbody components were always fixed to the EPIC 0.3–10 keV fits (Table 2) each time we ignored EPIC data between 0.33–1.77 keV, resulting in parameters consistent with the continuum modelling.

By alternatively excluding one particular plasma component from the spectral model we estimated the relative contribution to the spectral fit and the minimum  $\Delta C$ -stat improvement of each component for both the wind and jet model (see  $\Delta C^e$  values in Table 3). Following Pinto et al. (2020b), we compared the minimum  $\Delta C$ -stat values with the

**Table 3.** NGC 247 ULX-1: alternative plasma models.

Model 1	Parameter	Emission	Absorption
PIE (wind)	$L_X(E)$ , $N_H(A)$	$1.4 \pm 0.2$	$2.8 \pm 0.1$
	$\log \xi$ (erg/s cm)	$3.7 \pm 0.1$	$4.3 \pm 0.1$
	$v_{\text{LOS}}$ (c)	$+0.042 \pm 0.004$	$-0.166 \pm 0.002$
	$v_{\text{RMS}}$ (km/s)	$3000^{+2700}_{-800}$	$400 \pm 200$
	$\Delta C^a(e)$	104(97)	46(32)
	$\sigma^a(e)$	$> 5(> 5)$	$> 5(> 4)$
Model 2	Parameter	Emission	Absorption
CIE (jet)	$L_X(E)$ , $N_H(A)$	$1.4 \pm 0.2$	$2.5 \pm 0.1$
	$kT$ (keV)	$0.9 \pm 0.1$	$1.3 \pm 0.1$
	$v_{\text{LOS}}$ (c)	$-0.022 \pm 0.002$	$-0.168 \pm 0.003$
	$v_{\text{RMS}}$ (km/s)	$3000^{+3000}_{-1000}$	$1600 \pm 850$
	$\Delta C^a(e)$	83(51)	48(32)
	$\sigma^a(e)$	$> 5(> 5)$	$> 5(> 4)$

Main properties of the plasma components for two alternative models. Model 1 or PIE/wind: photoionised emission (*pion*) and absorption (*xabs*, see Fig. 10 and Fig. 11). Model 2 or CIE/jet: collisionally-ionised emission (*cie*) and absorption (*hot*, see Fig. 9). The column densities,  $N_H$ , are in units of  $10^{22} \text{ cm}^{-2}$ . The line-of-sight velocities,  $v_{\text{LOS}}$ , are in units of light speed  $c$ ; the velocity dispersion,  $v_{\text{RMS}}$ , is in  $\text{km s}^{-1}$ . The 0.3–10 keV luminosities of the emitting plasmas,  $L_X(E)$ , are defined in units of  $10^{38} \text{ erg/s}$ . The  $\Delta C^a(e)$  refer to the  $\Delta C$ -statistics of each component computed when the component is the only one in model (a) or when the other one is included (e). The same applies to the detection significances,  $\sigma^a(e)$ , evaluated with Monte Carlo simulations.

Montecarlo simulations to obtain an approximate estimate of the minimum significance of each wind or jet component (parameter  $\sigma^e$ ), which is highest for the emission phases.

Finally, to further test the strength of our results we performed a fit of the RGS and EPIC data including the whole EPIC energy band but fixing the plasma models to the best-fit results of the hybrid RGS (0.33–2 keV) plus EPIC (1.77–10 keV) fits. In Sect. 3.5.3, we noted that the inclusion of the photoionised *xabs* absorption component significantly decreased the C-stat from 4488 (of the simple 3-blackbody model) to 3033. The addition of the photoionised *pion* emission component further lowered the C-stat to 2431 (with a  $\chi^2 = 1830$  and a total of 1132 degrees of freedom). We performed the same fit by using instead the RGS jet model with

**Table 4.** NGC 247 ULX-1: continuum and plasma models

Model	RGS+EPIC ( $> 1.77$ keV)	RGS+EPIC (full band)
<i>3 bb</i>	2019/994	4488/1132
<i>3 bb * hot</i>	1971/990	3043/1132 gas par fixed
<i>3 bb * hot + cie</i>	1895/886	2542/1132 gas par fixed 2233/1124
<i>3 bb * xabs</i>	1973/990	3033/1132 gas par fixed
<i>3 bb * xabs + pion</i>	1877/886	2431/1132 gas par fixed 2191/1124

C-stat/d.o.f. values for spectral continuum and plasma models. ‘gas par fixed’ means that for those fits the parameters of both emission and absorption components were fixed to the best-fit values obtained excluding EPIC data below 1.77 keV.

the *hot* collisionally-ionised component fixing the parameters to those in Table 3. This decreased the C-stat from 4488 to 3043, similarly to the photoionised absorber. The addition of a *cie* emission component (with fixed plasma parameters) implied a final C-stat = 2542, which is slightly worse than *pion* due to some positive residuals left around 0.9 keV that can also be seen in the RGS spectral modelling in Fig. 11.

We notice that all the spectral fits shown here are not formally acceptable (see Table 4), although the winds components provide significant improvements. One reason is the variability of the features, both of their centroids and relative strength (see Fig. 3 and 4). This means that more complex models would be required to correctly fit the lines. On the other hand, the winds are likely multiphase as shown by the low-temperature O VII clearly missed by our single phase model (see Fig. 11). This was already shown in Pinto et al. (2020b) and occurs in SS 433 too (see Appendix A3). Finally, some bad cross-calibration below 0.6 keV between the EPIC and RGS cameras further prevent us from obtaining fully acceptable fits (see Fig. 5).

## 4 DISCUSSION

It is still unclear how does the wind vary with the accretion rate and whether it has a major role in shaping ULX spectra. Pinto et al. (2020a,b) showed that the wind evolves with the changes in the continuum from the fainter, harder states to the brighter states, which implies a tight relationship between the source’s spectral continuum and wind appearance as observed by comparing winds in different ULXs.

Among the ULXs, the supersoft ultraluminous X-ray (SSUL) sources are particularly fascinating objects. The fact that such sources reach very high luminosities (several  $10^{39}$  erg/s) but always exhibiting very soft ( $kT \sim 0.1$  keV) spectra indicates that they are being observed at moderate-to-high inclination angles as also suggested by the presence of dips in their lightcurves (see, *e.g.*, Feng et al. 2016). In fact, Urquhart & Soria (2016) modelled the soft X-ray residuals and the  $\sim 1$  keV drop found in several CCD spectra of ULXs with a model of thermal emission and an absorption edge, which they interpreted as a result of absorption and photon reprocessing by an optically-thick wind which obscures the innermost regions where most hard X-rays are produced.

### 4.1 Time evolution of the 1 keV residuals

The stacked XMM-*Newton* lightcurve (see Fig. 2) shows different pattern of source variability such as a long-term overall change in the average flux on daily time scales followed by abrupt drops in the flux where the source becomes softer (the dips) on timescales between 100s and a few hours. The dipping activity seems also to enhance during observations with higher flux peaks. The higher flux might be associated with a higher local accretion rate, which then would increase the radiative force and launch optically-thick wind cloudlets in the line of sight, thereby obscuring the innermost regions of the disc responsible for the hard X-ray emission (as suggested by Urquhart & Soria 2016). More insights on the nature of the dips will be provided by Alston et al. (2021). This work shows that the dips in the higher flux observations preferentially occur on 5 and 10 ks timescales, which suggests that they are caused from obscuration at  $\sim 10^{4-5} R_G$ , where  $R_G$  is the Gravitational radius (if the timescales are associated with keplerian motion around a NS or a stellar-mass BH). Such a range is comparable to the distance that the 0.17c wind would travel on a time scale of 1 ks, suggesting a possible connection between them.

The high-quality EPIC spectra of the individual observations show a remarkable flux variability in the features around 1 keV (see Fig. 3). In order to quantify such variability, we modelled the two strongest absorption features around 0.7 and 1.2 keV, and the dominant emission-like feature at 1 keV with three Gaussian lines for the EPIC (MOS and pn) spectral of the individual observations. All lines show a distinct pattern with their energy centroids significantly blueshifted during the brightest observations (which also exhibit most dips and the highest variability, see Fig. 4). Interestingly, the fluxes of the high-energy lines (1 and 1.2 keV) significantly decrease during the dipping observations while the 0.7 keV line seems to strengthen (see Table A1). This would either suggest a different location of the three lines, with the 0.7 keV line coming from the outer and less obscured regions, or a change in the ionisation state of the absorber during the high-flux periods. This is similar to what was observed in NGC 1313 ULX-1 (Pinto et al. 2020b, Middleton et al. 2015b). A detailed study of the broadband spectra and residuals evolution will be shown by D’Ài et al. (in prep). The fact that the location and strength of the residuals vary on hourly timescales with the source flux provides strong evidence in support for a disc wind rather than emission from the local ULX bubble or the galactic ISM.

### 4.2 A wind or a jet?

#### 4.2.1 Emission lines

The time-average stacked RGS spectrum showed strong emission residuals near the transition energies of several ions such as O VII-VIII, Ne IX-X and Fe XVIII (see Fig. 7 and 8). The agreement between RGS and EPIC is corroborated by applying the wind model constrained using only RGS in the 0.33 – 1.77 keV band to the whole EPIC MOS and pn time-average spectra (see Table 4). Unfortunately, the He-like emission triples of *e.g.* O VII and Ne IX are not well resolved likely due to the stacking of RGS spectra from different observations that clearly showed some variability in the line centroid as discussed above. This limited our capabilities of

distinguishing between collisional and photoionisation, but the use of full plasma models provided some constraints.

By performing automated searches of plasma models in a large parameter space, we built probability contours for both collisionally-ionised and photoionised plasma emission models. The properties of the line-emitting gas are very similar to those of the Galactic super-Eddington source SS 433 with a low velocity along the line of sight and a mild 1 keV temperature which is expected by the strong Ne K and Fe L emission around 1 keV (see Fig. 9). It is well established that the emission lines of SS 433 are from the jet with the low velocity indicating that the precessing jet was at very high angle, close to 90 degrees, in the analysed observation. If the lines of NGC 247 ULX-1 were also from a variable jet, the observed low velocity would suggest that it is being viewed at high angle in agreement with the presence of dips.

The photoionisation emission models (*pion* component in *SPEX*, see Fig. 10) however provided a significantly higher improvement to the spectral fits and a better description of the emission lines (see Table 3 and Fig. 11). This together with the evolution of the lines with the source continuum would favour photoionisation equilibrium similarly to the emission lines in NGC 1313 ULX-1 (Pinto et al. 2020b).

Regardless of the adopted equilibrium state, the luminosity of the line-emission component is remarkably high ( $L_{0.3-10\text{ keV}} > 10^{38}$  erg/s), similarly to NGC 1313 ULX-1, NGC 5408 ULX-1 (Pinto et al. 2016), NGC 55 ULX-1 (Pinto et al. 2017), NGC 5204 ULX-1 (Kosec et al. 2018a) and other ULXs (e.g., Wang et al. 2019). This is about 2-3 orders of magnitude higher than the emission lines in SS 433 and those producing the winds in classical supergiant X-ray binaries (sub-Eddington neutron stars accreting from supergiant OB stars, e.g. El Mellah & Casse 2017) or the lines from accretion disc coronae of low-mass X-ray binaries (see, e.g., Psaradaki et al. 2018). The luminosity of  $1.4 \times 10^{38}$  erg/s is instead comparable to the extended X-ray emission recently found around the extremely bright pulsating NGC 5907 ULX-1 (Belfiore et al. 2020), which suggests that the wind might be energetic enough to mechanically drive the  $\sim 100$ -pc super bubbles (see also Pinto et al. 2020a).

Similarly to NGC 1313 ULX-1, the O VII emission lines cannot be reproduced with the emission component responsible for the Fe L and Ne K emission (see Fig. 11). A second component (either photo- or collisionally-ionised) with a low blueshift of 6000 km/s would be required.

#### 4.2.2 Absorption lines

In this work we also reported a highly significant detection of mildly-relativistic, ultrafast, outflows. Both collisional and photoionisation (see Fig. 9, 10 and 11) plasma models identified a high velocity outflow ( $-0.17c$ ) in the range of the velocities found in other ULX winds.

The ionisation parameter is rather high ( $\log \xi = 4.3$ ) which is not surprising given the soft SED adopted for this source (see Fig. A3). If the wind at the launch is seeing a different SED (e.g., the hot innermost regions presumably obscured along our line of sight) the overall ionisation balance might be significantly different. This subject was extensively discussed in Pinto et al. (2020a) who found larger instability branches in the *S* curves of harder ULXs. Therefore, as a test, we performed an additional fit with the photoionised

*pion* + *xabs* wind model (as previously done in Sect. 3.6) by adopting the ionisation balance calculated for the hard state of NGC 1313 ULX-1 in Pinto et al. (2020b) to estimate the systematic effects on the wind parameters. The fit was statistically indistinguishable from the one performed with the ionisation balance computed for NGC 247 ULX-1, with the exception of the ionisation parameters which, as expected, turned out to be significantly lower by about  $\Delta \log \xi \sim 1$ .

The absorption lines are generally weaker than the emission lines in the RGS spectrum of NGC 247 ULX-1 which could be due to the low source continuum (Kosec et al. submitted). This was also predicted by Pinto et al. (2017) as the lines are normally seen on top of the continuum from the innermost regions which in this case is likely obscured.

Statistically we cannot distinguish photoionisation from collisional ionisation, but the former is favoured by the photoionised nature of the emitting plasma and the unusual detection of collisionally-ionised absorption in XRB winds.

### 4.3 Accretion disc and wind physics

In the framework of super-Eddington accretion the luminosity scales with the logarithm of the accretion rate in Eddington units ( $\dot{m} = \dot{M}/\dot{M}_E$ ) times the geometrical beaming of the funnel created by the height of the disc around the spherisation radius and by the wind itself (see Fig. 12). Following King & Lasota (2020), the apparent luminosity can be expressed with  $L_{\text{app}} = L/b = L_E(1 + \ln \dot{m})/b$ , where  $L$  is the intrinsic luminosity,  $L_E$  the luminosity in Eddington units, and  $b = 73/\dot{m}^2$  the geometrical beaming.

To estimate the bolometric luminosity of NGC 247 ULX-1 we integrated the broadband SED between 1 eV and 10 keV (or  $2.4 \times 10^{14-18}$  Hz, see Fig. A3) and obtained  $9.4 \times 10^{39}$  erg/s. NGC 247 ULX-1 luminosity could therefore be explained by assuming a black hole accreting above 10 times the Eddington rate or a neutron star accreting above  $\dot{m} = 25$ . At  $\dot{m} \sim 10$  the spherisation radius, *i.e.* the base of the wind, would be  $R_{\text{sph}} = 27/4\dot{m}R_G = 68R_G$ . Interestingly, this is very close to the escape radius for a  $-0.17c$  wind ( $R_e = 2GM/v^2 = 2R_Gc^2/v^2 = 73R_G$ ), which would indeed suggest that we detected a wind launched from the spherisation radius of a compact object above  $10 \dot{M}_E$ .

From Eq. (38) in Poutanen et al. (2007), assuming  $M_{\text{BH}} = 10M_\odot$  and  $\dot{m} = 10$ , we estimated a temperature for the spherisation radius  $T_{\text{sph}} \sim 0.3$  keV, which is comparable to the warm blackbody component in our fits (see Table 2), with the cooler ( $\sim 0.1$  keV) blackbody associated with the outer disc and, likely, the wind photosphere as suggested by recent work (see, e.g., Qiu & Feng 2021, Gúrpide et al. 2021). We notice, however, that the source is being seen at high inclination with a substantial fraction of the hard X-ray photons obscured by the funnel. The intrinsic luminosity of NGC 247 ULX-1 might therefore be higher than the value estimated above with a higher accretion rate, implying  $T_{\text{sph}} \sim 0.1 - 0.2$  keV, closer to the cooler blackbody component, and a slightly larger  $R_{\text{sph}}$ . It is also possible that the wind is launched with lower velocity at radii larger than  $73R_G$  and it gets accelerated by radiation pressure from the inner accretion flow (see, e.g., Takeuchi et al. 2013).

Similar considerations would apply to a non-magnetar ( $B \lesssim 10^{12}$  G) neutron star with  $\dot{m} = 25$  since the spherisation radius (in cm) would be of the same order of magnitude

as a  $10M_{\odot}$  black hole as both  $R_{\text{sph}}$  and  $T_{\text{sph}}$  scale with the  $\dot{M}$  and the mass of the compact object, whose trends nearly cancel out. This was briefly discussed in [Pinto et al. \(2020a\)](#).

The kinetic power of the wind can be written as  $L_w = 1/2 \dot{M}_w v_w^2 = 2\pi m_p \mu \Omega C v_w^3 / \xi L_{\text{ion}} \sim 4 \times 10^{40}$  erg/s, where  $\dot{M}_w = 4\pi R^2 \rho v_w^2 \Omega C$  is the outflow rate,  $\Omega$  and  $C$  are the solid angle and the volume filling factor (or *clumpiness*), respectively, which were adopted equal to 0.3 as conservative values from MHD simulations of winds driven by radiation pressure in super-Eddington winds ([Takeuchi et al. 2013](#)),  $\rho$  is the density and  $R$  is the distance from the ionising source. Here we have used the  $\xi$  definition to get rid of the  $R^2 \rho$  factor where  $\rho = n_{\text{H}} m_p \mu$  with  $m_p$  the proton mass and  $\mu = 0.6$  the average particle weight of a highly ionised plasma.

The filling factor of the wind might be much smaller. Using Eq. (23) in [Kobayashi et al. \(2018\)](#) and assuming that the outflow rate is comparable to the accretion rate, we obtain  $C \sim 3 \times 10^{-2}$ . Systematics would tend to cancel out when also accounting for the uncertainty on the ionisation parameter in the case for a harder SED ( $\Delta \log \xi \sim 1$ ). In the pessimistic case the wind power would be of the order of  $10^{39}$  erg/s, which means still high enough to affect the surrounding medium and inflate ISM cavities.

The spectral shape, strong wind features, and presence of dips suggest that NGC 247 ULX-1 is likely being observed at high inclination (see Fig. 12, left panel) where the funnel is already obscuring the innermost, hot, hard X-ray emitting regions. As mentioned in Sect. 4.1, the increase of the average flux level during the intermediate observations (3,4,5) might be caused by a higher local accretion rate. Such a climate change would however affect the properties of both the disc and the wind. The scale-height is already relevant around the Eddington limit (see, e.g., [Shakura & Sunyaev 1973](#), [Poutanen et al. 2007](#)). A further increase in the local  $\dot{M}$  might push the optically-thick funnel further upwards (see Fig. 12, right panel) thereby obscuring the regions emitting photons with temperatures higher than that of the spherisation radius ( $\gtrsim 0.3$  keV), causing the very soft dips shown in Fig. 2 (see also [Urquhart & Soria 2016](#)).

During the dips the high-ionisation portion of the wind could be hard to see as its absorption lines were primarily affecting the (now) obscured hard X-ray continuum. In fact, the strength of the high-ionisation (1.2-1.3 keV) absorption lines clearly decreases during the dipping observations (see Fig. 4), while the 0.7 keV O VIII absorption line seems constant in flux if not even stronger. This might also suggest a stratification in the wind. Outside the dips, an overall increase in the accretion rate would also imply a stronger radiative force and, therefore, a slightly faster wind which seems to be confirmed by the higher blueshift of the lines (see Fig. 3 and 4). The 1 keV emission lines also weaken during the bright / dipping observations, indicating that they should be produced in the inner regions in agreement with their overall larger broadening (see Table 3).

A similar picture was proposed by [Guo et al. \(2019\)](#) who argued that the  $\sim 100$ s transitions can be explained by the viscous timescale with the X-ray flux variability driven by accretion rate fluctuations (at  $\dot{m} \gtrsim 10$ ). However, local fluctuations in the  $\dot{M}$  might also cause variations in the winds, which could alter the source appearance ([Feng et al. 2016](#)).

Although fascinating and self-consistent, this scenario might be not the only one able to explain all the observables.

Additional, alternative, and (ideally) model-independent approaches could be considered. For instance, another phenomenon which might explain the nature of the dips might be the propeller effect due to a strong magnetic field. Such scenario would imply a decreasing  $\dot{M}$  and a geometrical beaming to cause the observed brightening. More insights on the temporal evolution of the spectral residuals accounting for the different spectral states that the source shows inside / outside the dips will be given in D’Ài et al. (in prep). Similarly, the Fourier analysis of the characteristics timescales in NGC 247 ULX-1 and the corresponding association with the dipping activity will be shown by [Alston et al. \(2021\)](#). Here, in particular, we argue that the alternation of the dips might be due to azimuthally-dependent structures.

We plan to investigate the variability of the RGS spectral lines to place more constraints onto their nature. However, the low count rate of the grating spectra currently prevent us from trying to study them during the dips and on timescales shorter than 100 ks in the bright states outside the dips. Future missions like XRISM and Athena will revolutionise the study of ULX thanks to their high effective area, high spectral resolution, and low background (see, e.g., [Barret et al. 2018](#), [Guainazzi & Tashiro 2018](#)). [Pinto et al. \(2020b\)](#) simulated NGC 1313 ULX-1 microcalorimeter spectra for these two missions and showed 1) how XRISM will strengthen the identification of lines in the 1 – 10 keV band and 2) how Athena / X-IFU will be able to detect winds in observations with just 1 ks of exposure time. The latter is primarily due to the fact that X-IFU will have two orders of magnitude higher effective area than RGS.

## 5 CONCLUSIONS

Most ULXs are believed to be powered by super-Eddington accreting neutron stars and, perhaps, black holes. The disc is expected to thicken at accretion rates above the Eddington rate and to launch powerful winds through radiation pressure and/or magnetic fields. Evidence of winds has been found in several ULXs through high-resolution X-ray spectrometers. It is yet unclear whether the switch between the classical soft and supersoft state - which is observed in supersoft ULXs - is due to the thickening of the disc and/or the optically-thick part of the wind. In order to better understand such phenomenology and the overall super-Eddington mechanism, we undertook a large observing campaign with XMM-Newton to study NGC 247 ULX-1, which is the brightest (in flux) of all supersoft ULXs.

The new observations showed for the first time unambiguous evidence of a wind in the form of emission and absorption lines from highly-ionised ionic species, with the absorption phase exhibiting a mildly-relativistic outflow ( $-0.17c$ ) in line with the other ULXs whose grating spectra had sufficient quality to detect and identify spectral lines. Remarkable variability was observed in the source flux with strong dipping activity during the brightest observations, which is typical among soft ULXs such as NGC 55 ULX-1, and indicate a close relationship between the accretion rate and the appearance of the dips. The latter are likely due to a thickening of the disc scale-height and the wind as shown by a progressively increasing blueshift in the spectral lines.

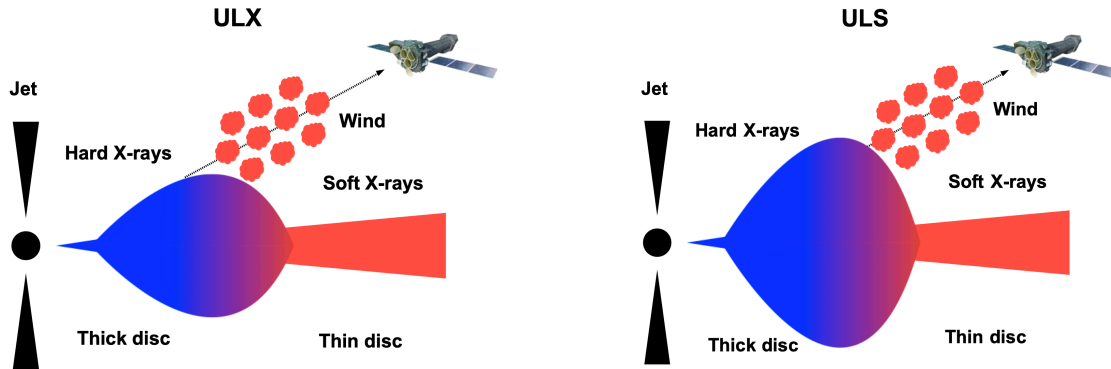


**Figure 12.** A possible scenario for the dips and ULX-ULS transitions in NGC 247 ULX-1. The source is observed at a viewing angle that is high enough that the inner disc is already partly obscured by the wind (soft ULXs, left panel). An increase of the accretion rate pushes up the scale-height of the disc and the optically-thick base of the wind, causing a near-total obscuration of the inner regions and the source appears as an ultraluminous supersoft source (ULS, right panel, see also Pinto et al. 2017, 2020b, Guo et al. 2019).

## ACKNOWLEDGMENTS

This work is based on observations obtained with XMM-Newton, an ESA science mission funded by ESA Member States and USA (NASA). We acknowledge support from ESA Research Fellowships. We thank the XMM-Newton SOC for support in optimising our observing campaign and J. M. Miller, D. Proga and M. Parker for useful discussion regarding winds and absorption in Galactic X-ray binary. AD, MDS, EA acknowledge financial support from the agreement ASI-INAF n.2017-14-H.0 and INAF main-stream. We thank the anonymous referee for their very useful suggestions.

## DATA AVAILABILITY

All of the data and software used in this work are publicly available from ESA’s XMM-Newton Science Archive (XSA<sup>1</sup>) and NASA’s HEASARC archive<sup>2</sup>. Our codes are publicly available and can be found on the GitHub<sup>3</sup>.

## REFERENCES

- Allevato V., Paolillo M., Papadakis I., Pinto C., 2013, *ApJ*, 771, 9
- Alston W. N., Pinto C., Barret D., D’Ai A., Del Santo M., et al., 2021, *MNRAS* in press, p. arXiv:2104.11163
- Bachetti M., Harrison F. A., Walton D. J., Grefenstette B. W., Chakrabarty D., et al., 2014, *Nature*, 514, 202
- Barret D., Lam Trong T., den Herder J.-W., Piro L., et al., 2018, in *SPIE Vol. 10699 of Society of Photo-Optical Inst. Eng. (SPIE) Conf. Series, The ATHENA X-ray Integral Field Unit (X-IFU)*. p. 106991G
- Begelman M. C., King A. R., Pringle J. E., 2006, *MNRAS*, 370, 399
- Belfiore A., Esposito P., Pintore F., Novara G., et al., 2020, *Nature Astronomy*, 4, 147
- Brightman M., Harrison F., Walton D. J., Fuerst F., Hornschemeier A., et al., 2016, *ApJ*, 816, 60
- Brinkmann W., Aschenbach B., Kawai N., 1996, *A&A*, 312, 306
- Cash W., 1979, *ApJ*, 228, 939
- Earnshaw H. M., Roberts T. P., 2017, *MNRAS*, 467, 2690
- El Mellah I., Casse F., 2017, *MNRAS*, 467, 2585
- Fabrika S., 2004, *ASPR*, 12, 1
- Feng H., Tao L., Kaaret P., Grisé F., 2016, *ApJ*, 831, 117
- Gladstone J. C., Roberts T. P., Done C., 2009, *MNRAS*, 397, 1836
- Goad M. R., Roberts T. P., Reeves J. N., Uttley P., 2006, *MNRAS*, 365, 191
- Guainazzi M., Tashiro M. S., 2018, *ArXiv e-prints*
- Guo J., Sun M., Gu W.-M., Yi T., 2019, *MNRAS*, 485, 2558
- Gürpide A., Godet O., Koliopanos F., Webb N., Olive J.-F., 2021, *arXiv e-prints*, p. arXiv:2102.11159
- Kaaret P., Feng H., Roberts T. P., 2017, *ARA&A*, 55, 303
- Kaastra J. S., 2017, *A&A*, 605, A51
- Kaastra J. S., Mewe R., Nieuwenhuijzen H., 1996, in K. Yamashita & T. Watanabe ed., *UV and X-ray Spec. of Astr. and Lab. Plasmas SPEX: a new code for spectral analysis of X & UV spectra..* p. 411
- King A., Lasota J.-P., 2020, *MNRAS*, 494, 3611
- King A. R., Davies M. B., Ward M. J., Fabbiano G., Elvis M., 2001, *ApJ*, 552, L109
- Kobayashi H., Ohsuga K., Takahashi H. R., Kawashima T., Asahina Y., Takeuchi S., Mineshige S., 2018, *PASJ*, 70, 22
- Koliopanos F., Vasilopoulos G., Godet O., Bachetti M., Webb N. A., Barret D., 2017, *A&A*, 608, A47
- Kosec P., Pinto C., Fabian A. C., Walton D. J., 2018a, *MNRAS*, 473, 5680
- Kosec P., Pinto C., Walton D. J., et al., 2018b, *MNRAS*, 479, 3978
- Kosec P., Zoghbi A., Walton D. J., Pinto C., Fabian A. C., Parker M. L., Reynolds C. S., 2020, *MNRAS*, 495, 4769
- Krautter J., Oegelman H., Starrfield S., Wichmann R., Pfeffermann E., 1996, *ApJ*, 456, 788
- Krolik J. H., McKee C. F., Tarter C. B., 1981, *ApJ*, 249, 422
- Liu J.-F., 2008, *ApJS*, 177, 181
- Marshall H. L., Canizares C. R., Hillwig T., Mioduszewski A., Rupen M., et al., 2013, *ApJ*, 775, 75
- Marshall H. L., Canizares C. R., Schulz N. S., 2002, *ApJ*,

<sup>1</sup> <https://www.cosmos.esa.int/web/xmm-newton/xsa>

<sup>2</sup> <https://heasarc.gsfc.nasa.gov/>

<sup>3</sup> <https://github.com/ciropinto1982>

564, 941

Medvedev P., Khabibullin I., Sazonov S., 2020, arXiv e-prints, p. arXiv:2005.12416

Medvedev P. S., Khabibullin I. I., Sazonov S. Y., Churazov E. M., Tsygankov S. S., 2018, *Astronomy Letters*, 44, 390

Middleton M. J., Heil L., Pintore F., Walton D. J., Roberts T. P., 2015a, *MNRAS*, 447, 3243

Middleton M. J., Roberts T. P., Done C., Jackson F. E., 2011, *MNRAS*, 411, 644

Middleton M. J., Walton D. J., Alston W., Dauser T., Eikenberry S., et al., 2018, arXiv e-prints, p. arXiv:1810.10518

Middleton M. J., Walton D. J., Fabian A., Roberts T. P., Heil L., Pinto C., et al., 2015b, *MNRAS*, 454, 3134

Miller J. M., Cackett E. M., Reis R. C., 2009, *ApJ*, 707, L77

Nandra K., George I. M., Mushotzky R. F., Turner T. J., Yaqoob T., 1997, *ApJ*, 476, 70

Pinto C., Alston W., Soria R., Middleton M. J., Walton D. J., et al., 2017, *MNRAS*, 468, 2865

Pinto C., Kaastra J. S., Costantini E., de Vries C., 2013, *A&A*, 551, A25

Pinto C., Mehdipour M., Walton D. J., Middleton M. J., Roberts T. P., et al., 2020a, *MNRAS*, 491, 5702

Pinto C., Middleton M. J., Fabian A. C., 2016, *Nature*, 533, 64

Pinto C., Ness J.-U., Verbunt F., Kaastra J. S., Costantini E., Detmers R. G., 2012, *A&A*, 543, A134

Pinto C., Walton D. J., Kara E., Parker M. L., Soria R., et al., 2020b, *MNRAS*, 492, 4646

Pintore F., Esposito P., Zampieri L., Motta S., Wolter A., 2015, *MNRAS*, 448, 1153

Poutanen J., Lipunova G., Fabrika S., Butkevich A. G., Abolmasov P., 2007, *MNRAS*, 377, 1187

Psaradaki I., Costantini E., Mehdipour M., Díaz Trigo M., 2018, *A&A*, 620, A129

Qiu Y., Feng H., 2021, *ApJ*, 906, 36

Shakura N. I., Sunyaev R. A., 1973, *A&A*, 24, 337

Soria R., Motch C., Read A. M., Stevens I. R., 2004, *A&A*, 423, 955

Stobbart A.-M., Roberts T. P., Wilms J., 2006, *MNRAS*, 368, 397

Sutton A. D., Roberts T. P., Middleton M. J., 2013, *MNRAS*, 435, 1758

Takeuchi S., Ohsuga K., Mineshige S., 2013, *PASJ*, 65, 88

Tarter C. B., Tucker W. H., Salpeter E. E., 1969, *ApJ*, 156, 943

Urquhart R., Soria R., 2016, *MNRAS*, 456, 1859

Vaughan S., Edelson R., Warwick R. S., Uttley P., 2003, *MNRAS*, 345, 1271

Walton D. J., Fürst F., Harrison F. A., Stern D., Bachetti M., et al., 2018c, *MNRAS*, 473, 4360

Walton D. J., Fürst F., Heida M., Harrison F. A., Barret D., et al., 2018a, *ApJ*, 856, 128

Walton D. J., Harrison F. A., Grefenstette B. W., Miller J. M., Bachetti M., et al., 2014, *ApJ*, 793, 21

Walton D. J., Mooley K., King A. L., Tomsick J. A., Miller J. M., et al., 2017, *ApJ*, 839, 110

Wang C., Soria R., Wang J., 2019, *ApJ*, 883, 44

## APPENDIX A: TECHNICAL DETAILS

In this section we put technical detail, plots, and tables, that were excluded from the main body of the paper.

### A1 Nearby bright X-ray source

The RGS extraction region includes a few faint sources with the brightest one being XMMU J004710.0-204708 (X-2 hereafter, see Fig. 1). We extracted its EPIC spectra from all observations and stacked them similarly to ULX-1. The spectrum of X-2 is much flatter than that of the ULX-1 and can be well modelled with a powerlaw model ( $\Gamma = 1.60 \pm 0.03$ ), a moderate column density  $N_{\text{H}} = (1.0 \pm 0.1) \times 10^{21} \text{ cm}^{-2}$ , and an intrinsic luminosity  $L_{0.3-10\text{keV}} = (1.45 \pm 0.04) \times 10^{38} \text{ erg/s}$  (assuming a distance of 3.3 Mpc). This corresponds to the Eddington limit for a Solar-mass star and, given the spectral slope, the source X-2 could be a common XRB near the NGC 247 centre. At 1 keV its spectrum is remarkably featureless and 40-50 times fainter than ULX-1 implying that it will have no significant effects on the RGS spectral lines.

### A2 Modelling of individual EPIC observations

Table A1 shows the results of the EPIC spectral modelling and the root-mean square estimated from the EPIC-pn data of each observation (see Sect. 3.1 and 2.1.4).

### A3 CIE model scan for the SS 433 RGS spectrum

We analysed the XMM-Newton RGS spectrum of SS 433 from the observation id:0694870201 (2012-10-03), which provides the longest ( $\sim 130$  ks) and best-exposed RGS spectrum of SS 433. We reduced the RGS spectrum of SS 433 obsid 0694870201 identically to that of the NGC 247 ULX-1 data shown in Sect. 2.1.2. After removing the very little Solar flares we are left with 129.4 ks for both RGS 1 and 2 cameras. We used the 6–25 Å range because at higher wavelengths the source emission is significantly absorbed and the background noise dominates the RGS spectrum (see Fig. A1). No significant pile up was found in the RGS spectra.

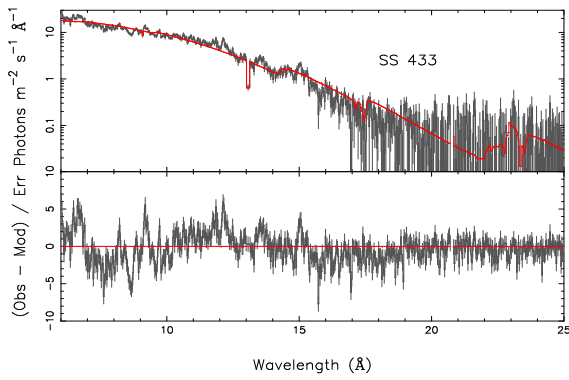
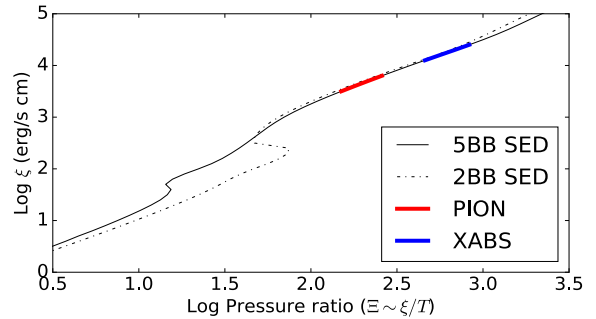
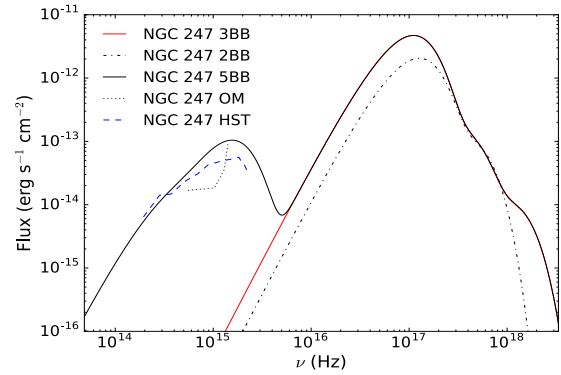
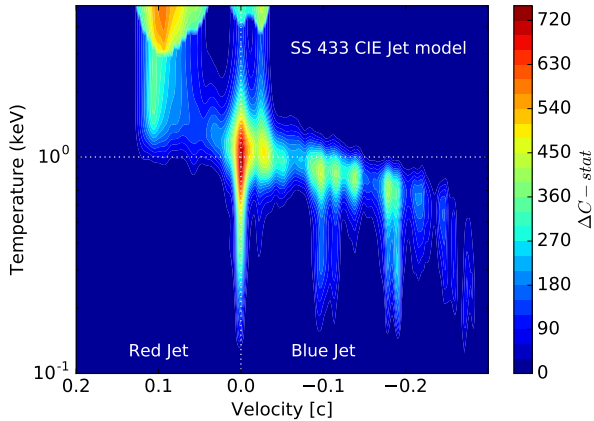
Strong emission lines were observed close to the rest-frame energies of the most relevant transitions such as Si XIII, Mg XI, Ne X, Ne IX, Fe XVII, and O VIII, which is very similar to NGC247 ULX-1, albeit at higher significance because SS 433 is much closer ( $\sim 5$  kpc) and brighter. We modelled the RGS spectral continuum with an absorbed powerlaw model obtaining results similar to Marshall et al. (2013) and Medvedev et al. (2018) such as a column density  $N_{\text{H}} = (1.14 \pm 0.02) \times 10^{22} \text{ cm}^{-2}$ , a slope  $\Gamma = 2.53 \pm 0.06$  and an X-ray unabsorbed luminosity  $L_{[0.3-10\text{keV}]} = (1.03 \pm 0.05) \times 10^{36} \text{ erg/s}$ . We obtained high C-stat/d.o.f = 2393/618 as expected, due to the strong, unmodelled, emission lines.

We tested onto the SS 433 RGS spectrum the same routine used for the NGC 247 ULX-1 data in Sect. 3.4.2 to check the robustness of our method. We adopted collisional ionisation equilibrium (*cie* model in *SPEX*) to model the jet emission. The velocity dispersion was fixed to 500 km/s, *i.e.* close to the RGS spectral resolution, the abundances were chosen to be Solar (to limit the computing time). We found a dominant low-velocity solution with an average temperature of 1 keV (see dotted horizontal and vertical lines in Fig. A2).

**Table A1.** Broadband properties of the individual observations.

Parameter	Spectra Model : $hot(bb + bb) + (gaus + gaus + gaus)$												Lightcurve	
	Blackbody 1		Blackbody 2		0.3-10keV	Gaussian 1		Gaussian 2		Gaussian 3		0.3-10keV	0.3-10keV	
	Area	Temp	Area	Temp	$L_{X,tot}$	Norm	Energy	Norm	Energy	Norm	Energy	$C/d.o.f.$	RMS	
Units	$10^{19}\text{cm}^2$	$10^{-1}\text{keV}$	$10^{16}\text{cm}^2$	$10^{-1}\text{keV}$	$10^{39}\text{erg/s}$	$10^{46}\text{ph/s}$	$10^{-1}\text{keV}$	$10^{46}\text{ph/s}$	$10^{-1}\text{keV}$	$10^{45}\text{ph/s}$	$10^{-1}\text{keV}$		(%)	
0844860101	$0.9 \pm 0.1$	$1.38 \pm 0.02$	$1.1 \pm 0.3$	$3.7 \pm 0.1$	$2.9 \pm 0.4$	$-1.2 \pm 0.2$	$6.9 \pm 0.1$	$1.5 \pm 0.2$	$9.5 \pm 0.1$	$-6.9 \pm 0.8$	$12.4 \pm 0.1$	321/160	$16.1 \pm 0.1$	
0844860201	$1.0 \pm 0.1$	$1.31 \pm 0.02$	$0.7 \pm 0.2$	$3.5 \pm 0.2$	$2.3 \pm 0.3$	$-0.9 \pm 0.2$	$6.7 \pm 0.1$	$1.8 \pm 0.2$	$9.3 \pm 0.1$	$-5.1 \pm 0.6$	$12.6 \pm 0.1$	341/140	$11.7 \pm 0.1$	
0844860301	$1.8 \pm 0.2$	$1.21 \pm 0.02$	$0.6 \pm 0.2$	$3.3 \pm 0.2$	$2.8 \pm 0.4$	$-1.3 \pm 0.2$	$6.6 \pm 0.1$	$2.6 \pm 0.2$	$9.1 \pm 0.1$	$-6.6 \pm 0.5$	$12.4 \pm 0.1$	441/128	$9.5 \pm 0.1$	
0844860401	$0.6 \pm 0.1$	$1.50 \pm 0.03$	$1.0 \pm 0.1$	$4.3 \pm 0.1$	$2.7 \pm 0.3$	$-1.4 \pm 0.2$	$7.5 \pm 0.1$	$0.8 \pm 0.2$	$9.9 \pm 0.1$	$-2.8 \pm 1.0$	$12.1 \pm 0.2$	412/192	$47.7 \pm 0.2$	
0844860501	$0.6 \pm 0.1$	$1.53 \pm 0.03$	$1.0 \pm 0.2$	$4.2 \pm 0.1$	$2.9 \pm 0.3$	$-1.7 \pm 0.2$	$7.4 \pm 0.1$	$0.6 \pm 0.2$	$9.8 \pm 0.2$	$-3.0 \pm 0.9$	$13.0 \pm 0.2$	391/188	$26.9 \pm 0.2$	
0844860601	$0.5 \pm 0.1$	$1.47 \pm 0.03$	$0.6 \pm 0.2$	$4.1 \pm 0.2$	$2.2 \pm 0.3$	$-1.1 \pm 0.2$	$7.2 \pm 0.2$	$0.6 \pm 0.2$	$9.8 \pm 0.2$	$-3.7 \pm 0.9$	$12.6 \pm 0.2$	271/154	$54.7 \pm 0.2$	
0844860701	$1.8 \pm 0.2$	$1.20 \pm 0.02$	$0.2 \pm 0.1$	$3.9 \pm 0.3$	$2.8 \pm 0.3$	$-1.1 \pm 0.3$	$6.5 \pm 0.2$	$2.2 \pm 0.2$	$9.0 \pm 0.1$	$-5.8 \pm 0.6$	$11.8 \pm 0.2$	324/122	$11.3 \pm 0.1$	
0844860801	$1.8 \pm 0.2$	$1.21 \pm 0.02$	$0.5 \pm 0.3$	$3.4 \pm 0.3$	$2.8 \pm 0.4$	$-1.9 \pm 0.3$	$6.6 \pm 0.1$	$2.0 \pm 0.2$	$9.2 \pm 0.1$	$-7.2 \pm 0.7$	$12.2 \pm 0.1$	298/109	$11.3 \pm 0.1$	

$L_X(0.3-10\text{keV})$  luminosities are calculated assuming a distance of 3.3 Mpc and are corrected for absorption (or de-absorbed, see Fig. 3).


**Figure A1.** SS 433 RGS spectrum and continuum model.

**Figure A3.** SED (top panel) and thermal-stability curve (bottom panel) computed for the time-averaged spectrum of NGC 247 ULX-1. The baseline SED (solid black line) consists of five unabsorbed blackbody models that account for emission in the optical, UV and X-ray bands. An alternative, simpler SED model uses just the X-ray two-blackbody model (dashed-dotted line).

**Figure A2.** Multi-dimensional scan of collisional-ionisation emission model for the SS 433 RGS spectrum. The X-axis shows the line-of-sight velocity. Labels are same as in Fig. 9.

The velocity is consistent with the dynamical range found by Medvedev et al. (2018) using the Fe K lines from the EPIC-pn spectrum, but showed a lower temperature, which is expected given that the RGS spectrum is more sensitive to the cooler gas phase of the multi-temperature jet.

#### A4 SED modelling and systematics effects

The non detection of the optical and UV counterpart of NGC 247 ULX-1 (Sect. 2.1.3) prevent us from building a simultaneous multi-wavelength SED for our source. This might have systematic effects on the calculation of the photoionisation balance. Moreover, the flux upper limits obtained with the OM suggest that at least in the far-UV en-

ergy band the source flux was lower than the levels measured in the archival HST observations that we used here.

Pinto et al. (2020a) showed that a lower IR-to-UV flux in moderately-hard sources, such as NGC 1313 ULX-1, mainly strengthens thermal instabilities at intermediate temperatures and ionisation parameters. In Fig. A3 we show the SED adopted here (solid black curve) consisting of a 5-blackbody model along with the simple 2-blackbody model (dashed-dotted black line, see also Sect. 3.5.1). The lower panel shows the stability curves computed for these models. Some deviations are mainly seen at  $\log \xi$  from 1.5–2.5, which is well below the values measured in this work (see Table 3). This is not surprising given the shortage of hard X-ray in our spectra which are the primary responsible of thermal instabilities. This suggests that the ionisation balance is not significantly affected even if the optical / UV fluxes were 2 orders of magnitude lower than our assumptions.

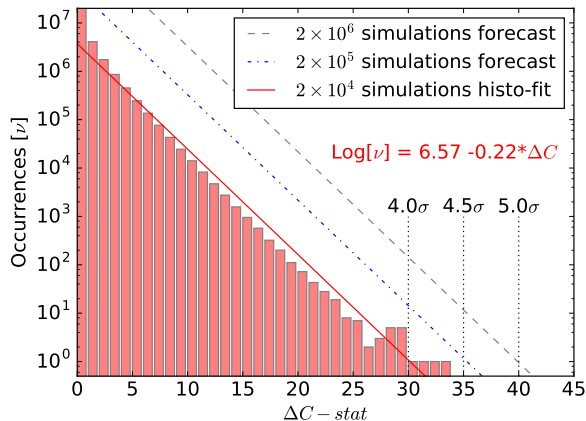


**Figure A4.** Histogram and corresponding power-law fit of the 20k Monte Carlo simulations of NGC 247 ULX-1 and forecast for 200 000 and 2 million simulations.

#### A5 Monte Carlo simulations and significance

The  $\Delta C_{\max}$  improvement to the continuum model does not necessarily yield the significance of the corresponding emission or absorption line models. This is due to the large parameter space that was explored and the possibility of detecting random spectral features (the look-elsewhere effect).

Among our physical model searches, the one for the absorption lines provided the smallest  $\Delta C_{\max}$  due to their strength being lower than that typical of the emission lines. We therefore focused on the results obtained with the *xabs* component and used them as a proxy for the *pion*.

Following the method used in Pinto et al. (2020b), we simulated 20 000 RGS and EPIC spectra adopting the 3-blackbody continuum model. Each faked spectrum was scanned with the same *xabs* grids used in Sect. 3.5.3. The results of our MC simulations are shown in Fig. A4. No outlier was found with  $\Delta C \geq \Delta C_{\max} = 46$ , which suggests a significance  $> 4\sigma$  for the absorbing gas.

We compared the simulations histogram for NGC 247 ULX-1 with those obtained for different sources by adopting a similar approach: 20k simulations of NGC 1313 ULX-1 (Pinto et al. 2020b), 2k for NGC 5204 ULX-1 (Kosec et al. 2018a) and 50k for the same data with a new, faster, cross-correlation method (Kosec et al. submitted), 20k for ULX NGC 7793 P13 (Pinto et al. in prep), and 1k for AGN PG 1448 (Kosec et al. 2020). We fit the histograms of the logarithm of the occurrences with straight lines and found an average slope  $\bar{\Gamma} = -0.225 \pm 0.015$ , which agrees with the simulations of NGC 247 ULX-1 ( $\Gamma = -0.218 \pm 0.006$ ).

We used the best-fit straight lines to estimate the overall shape of the  $\Delta C$ -stat distribution and forecast the results of larger numbers of simulations thanks to the agreement between the trends from 1 000 to 50 000 simulations. We therefore scaled the histogram fit of NGC 247 ULX-1, assuming a constant slope and multiplying the intercept of the straight line by a number equal to the ratio of the parameter space that we want to forecast for a given number of simulations and the one we obtained with 20 000 simulations. In Fig. A4 we show the predictions for  $2 \times 10^5$  (dash-dotted line) and  $2 \times 10^6$  (dashed line) simulations. This would suggest 4.5 and  $5\sigma$  detection probabilities for  $\Delta C$ -stat above 35 and 40, respectively, in the data with an uncertainty of  $0.2\sigma$  according to the spread in the slope of the other histograms.

We finally retrieved the various  $\Delta C$ -stat values that correspond to confidence levels ranging from 2.0, 2.5, ...,  $5.0\sigma$  and plot them as black contours in Fig. 10. The  $\sigma$  contours for the *pion* model scan were calculated by scaling the parameter space in the histogram of the *xabs* simulations in the same way used for the forecast.